

CHARACTERIZING BARS AT $Z \sim 0$ IN THE OSUBSGS: IMPLICATIONS FOR THE EVOLUTION OF BARRED GALAXIES

IRINA MARINOVA¹, SHARDHA JOGEE¹
 marinova@astro.as.utexas.edu, sj@astro.as.utexas.edu

Draft version April 28, 2019

ABSTRACT

Critical insights on galaxy evolution stem from studying local and high redshift bars. We present results on bars at $z \sim 0$, based on OSUBSGS B and H images of 180 spirals. (1) The deprojected bar fraction is 60% in H and 44% in B , confirming the ubiquity of local bars. The results before and after deprojection are almost identical, which is encouraging for high redshift studies. (2) Most ($\sim 71\%$) bars have moderate to high strengths or ellipticity ($0.50 \leq e_{\text{bar}} \leq 0.75$), and only a small fraction (7%–10%) are very weak ($0.25 \leq e_{\text{bar}} \leq 0.40$). There is no bimodality in the distribution of bar strengths. Both the bar fraction and bar strengths in H show no variation across RC3 Hubble types. Taken together, these results suggest that most bars in $z \sim 0$ galaxies are relatively robust against the range in central mass concentrations, gas mass fractions, and other host galaxy properties present along the Hubble sequence. (3) RC3 bar types should be used with caution. A significant fraction of galaxies that are classified as unbarred in RC3 turn out to be barred, and RC3 bar classes ‘B’ and ‘AB’ have a significant overlap in bar strength. (4) Most (72% in B and 76% in H) bars have sizes below 5 kpc. Bar and disk sizes correlate and the ratio (a_{bar}/R_{25}) lies primarily in the range 0.2 to 0.4. This suggests that the corotation resonance lies inside R_{25} and that the growths of bars and disks are intimately tied. (5) The fraction of bright disks ($M_V < -19.3$) that host strong ($e_{\text{bar}} \geq 0.4$) large-scale bars in the B band at $z \sim 0$ is $35 \pm 6\%$. This is comparable to the value of $\sim 30 \pm 6\%$ reported earlier for similar systems at $z \sim 0.2$ –1.0 or lookback times of 3–8 Gyr, thereby ruling out cosmogonies where the bar fraction declines strongly with redshift.

Subject headings: galaxies: fundamental parameters — galaxies: structure — galaxies: kinematics and dynamics — galaxies: evolution

1. INTRODUCTION

Stellar bars are recognized as the most important internal factor that redistributes the angular momentum of the baryonic and dark matter components of disk galaxies (e.g., Weinberg 1985; Debattista & Sellwood 1998, 2000; Athanassoula 2002; Berentzen, Shlosman, & Jogee 2006), thereby driving their dynamical and secular evolution. Bars efficiently drive gas from the outer disk to the central few hundred parsecs and are observed to feed central starbursts in local galaxies, (Elmegreen 1994; Knapen et al. 1995; Hunt & Malakan 1999; Jogee et al. 1999, Jogee, Scoville, & Kenney 2005). It remains a matter of contention whether large-scale bars relate to AGN activity in galaxies, given the reduction by several orders of magnitude needed in the specific angular momentum of gas before it can feed a central black hole, and conflicting observational results (see review by Jogee 2006 and references therein; also Mulchaey & Regan 1997; Knapen et al. 2000; Laine et al. 2002; Laurikainen et al. 2004). In several galaxies, bar-driven gas inflows appear intimately tied to the formation of disk, high v/σ stellar components in the inner kpc or ‘pseudobulges’ (Kormendy 1993; Jogee 1999; review by Kormendy & Kennicutt 2004, Jogee, Scoville, & Kenney 2005; Athanassoula 2005; Debattista et al. 2006). Furthermore, the orbital structure of bars can lead to the observed peanut-shaped and boxy bulges in inclined galaxies (Combes et al. 1990; Pfenniger and Norman 1990; Bureau & Athanassoula 2005; Athanassoula 2005; Martinez-Valpuesta et al. 2006; Debattista et al. 2006).

Earlier *Hubble Space Telescope (HST)* studies at optical wavelengths (e.g., Abraham et al. 1999) reported a paucity of stellar bars and a sharply declining optical bar fraction at intermediate redshifts $z > 0.5$. Studies at near-infrared (NIR) wavelengths had a large effective point spread functions (PSFs) and only detected large bars whose semi-major axes exceeded $0.9''$, corresponding to 7.2 kpc² at $z \sim 1.0$ (Sheth et al. 2003). Recent work based on large optical surveys have now established the abundance of bars at intermediate redshifts $z \sim 0.2$ –1.0, corresponding to lookback times of 3–8 Gyr (Elmegreen et al. 2004, hereafter E04; Jogee et al. 2004, hereafter J04; Zheng et al. 2005, hereafter Z05). The fundamental issue of how robust bars are, and the associated implications for bar-driven evolution in disks over the last 10 Gyr, remains open (e.g., J04; Shen & Sellwood 2004; Athanassoula, Lambert, & Dehnen 2005; Bournaud et al. 2005; Berentzen, Shlosman, & Jogee 2006; Martinez-Valpuesta et al. 2006; Debattista et al. 2006).

In order to put bars in a cosmological context, it now behooves us to characterize the frequency and impact of bars, by applying the *same quantitative* methods to large samples at $z \sim 0$ and at higher redshifts. Spurred by these considerations, we characterize in this paper the frequency and structural properties of bars in the local Universe at optical and NIR wavelengths, by ellipse-fitting the B and H images of the OSU Bright Spiral Galaxy Survey (OS-

¹ Department of Astronomy, University of Texas at Austin, 1 University Station C1400, Austin, TX 78712-0259

² We assume in this paper a flat cosmology with $\Omega_M = 1 - \Omega_\Lambda = 0.3$ and $H_0 = 70 \text{ km s}^{-1} \text{ Mpc}^{-1}$.

UBSGS; Eskridge et al. 2002) of 180 spirals. The first and main goal of this study is to provide *quantitative* characterizations of the bar fraction f_{bar} (defined as the fraction of disk galaxies that are barred) and structural properties (size, ellipticities, strength, etc.) of bars at $z \sim 0$, as a function of wavelength, Hubble types, and host galaxy properties. The second goal of our study is to provide a *rest-frame optical* $z \sim 0$ point for bars based on ellipse fits, in order to directly compare with studies of intermediate redshift bars (J04; E04; Z05) that also use ellipse fits. In particular, we use in this paper the same procedure of ellipse fits (§ 3.1) and the same quantitative characterizations (§ 3.3) of bars that were applied by J04 to bars at intermediate redshifts ($z \sim 0.2\text{--}1.0$) in the Galaxy Evolution from Morphology and SEDs (GEMS; Rix et al. 2004) survey.

Several studies have used the OSUBSGS to gauge bars in the local Universe (e.g., Block et al. 2002; Eskridge et al. 2000; Whyte et al. 2002; Buta et al. 2005), but they differ significantly from our study and cannot meet our two goals. Eskridge et al. (2000) visually classified bars in the H -band, and in the B -band, they used the Third Reference Catalog of Bright Galaxies (de Vaucouleurs et al. 1991; hereafter RC3) visual bar classes. Such visual classifications form an invaluable first step, but by definition, are subjective and difficult to compare with results from other studies. Block et al. (2002) and later Buta et al. (2005) applied the gravitational torque Q_b method, based on Fourier amplitudes, to H -band images of 163 and 147 OSUBSGS galaxies, respectively. This quantitative method is less subjective than visual classification, but the results of Block et al. (2002) and Buta et al. (2005) cannot be compared to intermediate redshift studies for two reasons. First, the latter studies were based on the *HST* Advanced Camera for Surveys (ACS) data and trace the rest-frame optical properties of bars, while Block et al. (2002) and Buta et al. (2005) deal with the rest-frame NIR. Secondly, it is non-trivial to derive Q_b for intermediate redshift galaxies due to resolution and signal-to-noise limitations. Whyte et al. (2002) fitted ellipses to B -band images of only 89 of the 180 OSUBSGS galaxies, and do not provide a distribution of bar sizes and strength, as a function of Hubble type and host galaxy properties. Our study complements these existing studies by ellipse fitting B -band and H -band images of all 180 OSUBSGS galaxies, and performing a comprehensive statistically significant analysis of barred galaxies in the local Universe.

The outline of this paper is as follows. § 2 discusses the sample selection based on the OSUBSGS survey (Eskridge et al. 2002). § 3 describes the ellipse-fitting method, the criteria used for identifying bars, and deprojection of images and profiles to face-on. In § 4.1–4.4, we present results on the bar fraction at $z \sim 0$, its dependence on Hubble type, the distribution of bar size and strengths, and the variation of bar properties along the Hubble sequence. Results are presented both before and after deprojection to face-on. In § 4.5, we discuss the constraints set by our results for theoretical models addressing the robustness of bars, and the assembly of the Hubble sequence over cosmological times. In § 4.6, we present a first-order comparison of the bar fraction and properties at $z \sim 0$ from OSUBSGS to those derived at intermediate redshift from GEMS

(J04). § 5 presents the summary and conclusions.

This paper is the first in a series of three based on the OSUBSGS. In paper II (Marinova et al. in prep), we will present simulations that artificially redshift the rest-frame optical and NIR images of the local OSUBSGS sample out to $z \sim 1\text{--}2$, in order to assess the impact of redshift-dependent systematic effects on the recovery rate of bars in surveys conducted by current and future facilities in the optical and IR, such as the planned Wide Field Camera 3 (WFC3) and the James Webb Space Telescopes (JWST). Paper III will address the bulge properties and activity of barred and unbarred galaxies in the OSUBSGS sample.

2. DATA AND SAMPLE

The OSUBSGS targets local spiral galaxies that are taken from the RC3 catalog and chosen to represent the bright disk galaxy population in the local universe (Eskridge et al. 2002). The galaxies are selected using the following criteria: RC3 type of S0/a or later, $(0 \leq T \leq 9)$, $M_B < 12$, $D_{25} < 6'.5$, and $-80^\circ < \delta < +50^\circ$ (Eskridge et al. 2002), and are imaged in B , V , R , H , J , and K bands. The B and H images of 182 OSUBSGS galaxies are available as part of a public data release (Eskridge et al. 2002). Our starting sample (sample S1) consists of the afore mentioned 182 OSUBSGS galaxies with B and/or H images. After discarding galaxies (2 galaxies or 1% of sample S1) that do not have images in both the B and H bands, we are left with sample S2 of 180 galaxies imaged in both bands. This constitutes the sample of galaxies to which we fitted ellipses in order to characterize bars and disks, as outlined in § 3.

3. METHOD FOR CHARACTERIZING BARS AND DISKS

We adopt the widely used procedure (e.g., Wozniak et al. 1995; Jogee et al. 1999, 2002a,b, 2004; Knapen et al. 2000; Laine et al. 2002) of characterizing bars and disks in galaxies via ellipse fits. Our analysis procedure is schematically illustrated in Figure 1 and described in sections 3.1 to 3.4.

3.1. Ellipse Fitting

We start with the sample S2 of 180 galaxies imaged in both B and H bands (Fig. 1). We first remove stars from the B and H band images of each galaxy, and find the center of the galaxy using the IRAF routine ‘imcenter’. We determine a maximum galaxy semi-major axis length (a_{max}) out to which ellipses will be fitted in each image by finding out where the galaxy isophotes reach the sky level. We then use the standard IRAF task ‘ellipse’ to fit ellipses to each image out to a_{max} . We employ an iterative wrapper developed by J04 to run ‘ellipse’ up to 300 times for each object in order to get a good fit across the whole galaxy. From the final fit for each galaxy, we generate radial profiles of surface brightness (SB), ellipticity (e), and position angle (PA). The fitted ellipses are overplotted onto the galaxy images to generate overlays. Examples of the radial plots and overlays are shown in Figures 2, 4, and 5. For each galaxy, an interactive visualization tool (J04) is used to display both the radial profile and the overlays in order to perform an extra inspection of the fits.

Of the 180 galaxies in sample S2, 179 (99%) and 169 (94%) were successfully fitted in the H and B -band, respectively. Of the 11 galaxies that could not be fitted in

the B band, 5 had strong morphological distortions and seem to be interacting; one had a very bright saturated star with leakage; and 5 had no clearly defined center. Further analyses to characterize inclined, unbarred, and barred disks in § 3.2 were then restricted to the sample S3 of 169 galaxies with successful fits in both the B and H bands (Fig. 1).

3.2. Identifying and excluding highly inclined spirals

For sample S3, we use the B band images, rather than the H band images, to identify and characterize the outer disk because the former are deeper and trace the disk farther out. From the radial profiles and ellipse overlays generated by ellipse-fitting the B -band image, we measure the ellipticity (e_{disk}) and PA (PA_{disk}) of the outer disk. The outer disk inclination, i , is derived from e_{disk} using $\cos(i) = (1 - e_{\text{disk}})$. Of the 169 galaxies in sample S3, we find 32 (19%) galaxies with disk inclination $i > 60^\circ$, and classify them as ‘inclined’. They are listed in the lower part of Table 1. Figure 2 shows an example of the B band radial profile and ellipse overlays for an inclined galaxy.

We only use the final sample S4 (Fig. 1) of 137 moderately inclined ($i < 60^\circ$) spirals to further characterize the properties of bars (e.g., size, strength, frequency) and unbarred disks in § 3.3–3.4. Such an inclination cutoff is routinely applied in morphological studies because projection effects make it very difficult to reliably trace structural features in a galaxy that is close to edge-on. The exclusion of highly inclined galaxies does not bias the distribution of Hubble types, as shown in Figure 3a, where Hubble types of samples S3 and S4 are compared. The absolute V-band magnitudes (M_V) of both sample S3 and S4 cover the range -18 to -24, with most galaxies lying in the range $M_V \sim -20$ to -22 (Fig. 3b).

3.3. Characterizing bars and disks without deprojection

In § 3.4, we will use the *deprojected* radial profiles of (SB, e , PA) to characterize the intrinsic properties of bars and disks in sample S4. However, we also decide to first perform the analysis on the *observed* radial profiles *before* deprojecting them to face-on. There are several reasons for this dual approach of deriving bar properties both before and after deprojection. Firstly, it is useful to have bar properties (e.g., frequency, strength, sizes) prior to deprojection, in order to compare directly to studies at intermediate redshifts (J04, E04, Z05), where deprojection is not done for several reasons, including the difficulty in accurately measuring the PA of the line of nodes and the inclination of the outer disk in noisy images of distant galaxies. Secondly, by having bar properties both before and after deprojection, we are able to assess whether deprojection makes a significant difference to the statistical distributions of bar properties. A large difference would raise concerns for intermediate redshift studies or even for large nearby studies where deprojection is often not carried out.

For sample S4, we use the observed radial profiles of (SB, e , PA) and the ellipse overlays, to classify galaxies as ‘unbarred’ (Fig. 4) or ‘barred’ (Fig. 5), according to the following quantitative criteria. A galaxy is classified as barred if it satisfies the following conditions: (1) the ellipticity e increases steadily to a global maximum e_{bar}

greater than 0.25, while the PA value remains constant (within 10°), and (2) the e then drops by at least 0.1 and the PA changes at the transition from the bar to the disk region. Criterion (1) is justified because the ellipse fits are a guide to the underlying stellar orbits. The main bar-supporting orbits are the ‘ x_1 ’ family, which are elongated along the bar, keeping the PA constant as a function of radius in the bar region. We choose a lower limit of 0.25 for the peak ellipticity, e_{bar} , of a feature before it is identified as a bar. Below this cutoff, structures are very round and even disks may contaminate the analysis. We also note that if we lower the cutoff from 0.25 to 0.10, we do not recover more ‘bars’ that would satisfy the conditions of a smooth rise in ellipticity and a flat PA plateau. The rationale for criterion (2) is that the disk is more circular than the bar for moderately inclined galaxies, and the disk and bar in general have a different PA. Furthermore, the requirement that the ellipticity drops by 0.1 at the transition from bar to disk has been shown to work well in identifying bars (e.g., Knapen et al. 2000; Laine et al. 2002; Jogee et al. 2002a, 2002b, 2004). Figures 4 and 5 show examples of an unbarred and barred galaxy, respectively.

In addition to classifying galaxies as ‘barred’ and ‘unbarred’, we also use the radial profiles to derive structural properties of the bar and disk. Specifically, for all galaxies, we measure the ellipticity, PA, and, semi major axis of the outer disk (e_{disk} , PA_{disk} , a_{disk}). For galaxies classified as ‘barred’, we also measure the corresponding quantities (e_{bar} , PA_{bar} , a_{bar}) for the bar. The maximum bar ellipticity, e_{bar} can be used as a measure of the bar strength based on simulations (Athanassoula 1992a; Athanassoula & Misiriotis 2002) and observed correlations between e_{bar} and the gravitational torque (Laurikainen et al. 2002).

We note that the ‘constant PA’ criterion that we use to identify bars may cause us to miss some weak bars at optical wavelengths due to the following reason. In weak bars, the shock loci and corresponding dust lanes on the leading edge of the bar are curved (Athanassoula 1992b). In optical images of weak bars, these curved dust lanes may cause the PA to twist or vary slightly along the bar, thereby preventing the ‘constant PA’ criterion from being met. In the case of very strong bars, the ‘constant PA’ criterion is a good one and isophotal twist is not an issue, because such bars have strong shocks and straight dust lanes along their leading edges (Athanassoula 1992b). In order to gauge how many bars we might be missing because of the ‘constant PA’ criterion, we identify galaxies that show a PA twist accompanied by an ellipticity maximum. It turns out that only a small fraction ($\sim 6\%$) of galaxies show this effect.

3.4. Characterizing bars and disks after deprojection

For sample S4, we use the inclination i and the PA of the outer disk (determined in § 3.2) to *analytically* deproject the observed H and B band radial profiles of (e , PA) to face-on. We perform the analytical deprojection using a code developed by Laine et al. (2002) and used previously in Laine et al. (2002) and Jogee et al. (2002a,b). It should be noted that the deprojection formula used in the code only strictly applies to infinitesimally thin structures, and may be inaccurate near the galaxy center in the vicinity of the bulge. However, it is a reasonable approximation in

the region of interest where large-scale bars reside. Figure 6 shows an example of the deprojected radial profiles of NGC 4548 in the B and H bands overlaid on the observed profiles.

We note that the process of analytically deprojecting the radial *profiles* to face-on after ellipse-fitting the observed (i.e. un-deprojected) images is analogous to the process of first deprojecting the observed *images* to face-on, and then ellipse-fitting the deprojected images in order to generate face-on radial *profiles*. We verified this expectation with the following steps. (1) We deproject the *images* of several galaxies using the Multichannel Image Reconstruction, Image Analysis and Display (MIRIAD) routine ‘de-project’. The routine takes as input the observed image, the galaxy center, the inclination i and PA of the outer disk, and outputs the deprojected image; (2) We then fit ellipses to these deprojected images using the procedure outlined in § 3.1, and generate face-on radial profiles of SB, e , and PA; (3) These face-on radial profiles generated from the deprojected images, are compared with the deprojected radial profiles derived analytically from the the observed profile. There is good agreement in all cases.

This is illustrated in Fig. 7 for the B band image of NGC 4548. The observed and deprojected images are shown in the left panel. In the right panel, 3 radial profiles are plotted: the observed radial profile derived by fitting ellipses to the observed image is plotted as stars; the deprojected radial profile derived analytically from the observed profile is plotted as squares; and the face-on radial profile derived by fitting ellipses to the deprojected image is plotted as triangles. There is good agreement between the squares and the triangles.

The deprojected profiles provide an accurate characterization of the ‘intrinsic’ or face-on properties of disks and bars. For all galaxies in S4, we therefore use the analytically deprojected B and H radial profiles to classify galaxies as ‘barred’ or ‘unbarred’, according to the criteria outlined in § 3.3. We also remeasure the bar ellipticity (e_{bar}), bar semi major axis (a_{bar}), and disk size a_{disk} , and verify that the disk ellipticity is close to zero in the deprojected radial profile. In the rest of this paper, many of these deprojected quantities will be compared to those derived before deprojection (§ 3.3) in order to gauge the impact of deprojection.

4. RESULTS AND DISCUSSIONS

4.1. The optical and NIR bar fraction at $z \sim 0$

Table 2 and Figure 8 show the bar fraction (defined as the fraction of spiral galaxies that are barred) for the B and H bands, both before (§ 3.3) and after deprojection (§ 3.4). The results are based on sample S4 of 137 moderately inclined ($i < 60^\circ$) spirals (§ 3.2). We find a deprojected bar fraction of 44% in the B -band and 60% in the H -band. The lower bar fraction in optical images is expected as they miss bars obscured by dust and star formation. Our results that 60% of spirals are barred in the infrared confirms the preponderance of bars among spirals in the local Universe. We check for a systematic bias of galaxy class as ‘barred’ or ‘unbarred’ with galaxy luminosity L_B and $B - V$ color and find no bias.

Our deprojected H -band bar fraction of 60% is consistent with the results, based on visual inspection of the H

band OSUBSGS images, by Eskridge et al. (2000). They find an overall H -band bar fraction of 72%, with 56% of spirals hosting ‘strong’ bars and 16% hosting ‘weak’ bars. We present a more detailed comparison of our bar strengths and fraction with other studies in § 4.3.

It is interesting that deprojection does not make any significant changes to the global bar fraction, when dealing with the fairly large OSUBSGS sample. As shown by Table 2 and Figure 8, the B and H band bar fractions are 42% and 58% before deprojection, and change by only a factor of 1.04 and 1.03, respectively, after deprojection. We suggest several reasons for the small impact of projection effects. Firstly, this study uses only moderately inclined ($i < 60^\circ$) galaxies where projection effects are less severe than in highly inclined systems. Secondly, projection effects produce large changes in the morphology of a galaxy only when the disk inclination i is significant *and* the difference in PA between the bar and the disk major axes is close to 90° . From a statistical point of view, these two conditions are unlikely to occur simultaneously in a dominant fraction of the sample. These arguments are supported by Figures 9a and 9b, which show that the galaxy classes assigned prior to deprojection are in no way biased by the galaxy inclination i : both ‘barred’ and ‘unbarred’ galaxies span a similar range in i . Furthermore, even the bar ellipticity e_{bar} measured before deprojection is uncorrelated with i (Figs. 9c and 9d).

The fact that the bar fraction in large samples is similar before and after deprojection is encouraging for large studies of bars at intermediate redshift (e.g., J04, E04, Z05), where deprojection is often not done because of the difficulty in accurately measuring the PA of the line of nodes and the inclination of the outer disk in noisy images of distant galaxies.

4.2. Sizes of bars and disks at $z \sim 0$

The distributions of bar sizes or semi-major axes (a_{bar}) before and after deprojection are shown for the B and H bands in Figure 10. Some bars do appear larger after deprojection, but from a statistical point of view, deprojection does not have a significant effect on the bar size distribution. Sizes of bars in the local Universe lie in the range ~ 1 to 14 kpc, with most (72% in B and 76% in H) bars having $a_{\text{bar}} \leq 5$ kpc, and $\sim 50\%$ of them clustering a_{bar} in the range 2 to 5 kpc. If such a distribution of bar sizes is present at a redshift $z \sim 1$, where 1'' corresponds to 8.0 kpc, then only observations with angular resolutions superior to 0''.3 can adequately resolve the majority of bars.

In Figure 11, we plot the bar size versus the disk size before and after deprojection. The bar size is measured in the H band where the low extinction enables more accurate measurement than in the optical. The disk is measured in the B band image, which is deeper than the H band and traces the disk further out (§ 3.2). Both before and after deprojection, we find that bar and disk sizes are correlated with an average slope of ~ 0.9 , albeit with a large scatter of several kpc in bar size at a given disk size.

Figure 12 shows the observed bar semi-major axis distribution normalized to R_{25} , (the radius in arcseconds of the isophote, where the surface brightness equals 25 mag arcsec $^{-2}$) of the disk. R_{25} values are obtained from

the NBG, except for NGC 6753, 6782, 5078, 6907, 7814, and ESO 142-19, which are from the RC3. The ratio (a_{bar}/R_{25}) lies primarily in the range 0.2 to 0.4 in both H and B bands (Fig. 12). This is consistent with the results of Menendez-Delmestre et al. (2004), who find an average (a_{bar}/R_{25}) ratio of 0.35, on the basis of ellipse fits of 134 2MASS galaxies. Erwin (2005) also finds a mean a_{bar}/R_{25} ratio of 0.38 and a correlation of bar size with disk size, but only for early-type S0-Sab galaxies, based on ellipse fits of 65 local galaxies imaged in the R -band.

What do these results imply? In theory, the size of the bar (a_{bar}) depends on the concentration of matter in the disk and the distribution of resonant material that can absorb angular momentum from the bar (Athanasoula 2003). If bars end near the the corotation resonance (CR), as is found observationally (e.g., Merrifield & Kuijken 1995; Debattista et al. 2002; Aguerri et al. 2003), then our result that (a_{bar}/R_{25}) is generally well below 1.0 suggests that the CR of disk galaxies lies well inside their R_{25} radius. The correlation between bar and disk sizes, and the narrow range in a_{bar}/R_{25} suggest that the growths of the bar and disk may be intimately tied.

4.3. Distribution of bar strengths at $z \sim 0$

Bar ‘strength’ can be an ambiguous term and studies using various methods of bar characterization define bar strength differently. A physically meaningful measure of the ‘strength’ of a bar might entail a measure of the inflow rate it can drive, and could be estimated by integrating the gravitational torque exerted by the bar as a function of radius. However, no such measure currently exists and bar strengths are estimated via several methods: visual inspection, the Q_b method (Block et al. 2002; Buta et al. 2005), the maximum ellipticity of the bar, bar/interbar contrasts, and Fourier decomposition techniques (Elmegreen & Elmegreen 1985; Elmegreen et al. 1996).

The Q_b method (Block et al. 2002; Buta et al. 2005) directly measures the gravitational torque exerted at the bar, but it measures the torque at only one point along the bar. The Q_b method depends on the scale height of the disk and the ability to derive a reliable model for the potential using images. It is hard to apply this method to a large number of intermediate redshift galaxies due to resolution and signal-to-noise limitations. In the bar/interbar contrast method used by Elmegreen & Elmegreen (1985) and Elmegreen et al. 1996, the bar strength is characterized by the ratio of the peak surface brightness in the bar region to the minimum surface brightness in the interbar region. The Fourier decomposition method also used by Elmegreen & Elmegreen (1985) and Elmegreen et al. (1996), is similar to the Q_b method. It characterizes bar strength by measuring the relative amplitudes of the Fourier components of the bar. The maximum amplitude of the $m=2$ mode determines the strength of a bar. When using ellipse fits to characterize bars, the maximum ellipticity of the bar (e_{bar}) is used as a measure of bar strength (e.g., Athanassoula 1992a; Wozniak et al. 1995; Jogee et al. 1999, 2002a,b; Knapen et al. 2000; Laine et al. 2002). The rationale is that fitted ellipses are a guide to the underlying stellar orbits supporting the bar, and a thin elongated bar with a high e_{bar} is expected to impose a large torque on the surrounding gas. Laurikainen et al.

(2002) find that Q_b and e_{bar} correlate up to moderate e_{bar} , but for high e_{bar} (> 0.6) the correlation is not linear.

In this study, we use the bar ellipticity e_{bar} as a measure of the bar strength. Figure 13 shows the observed and deprojected distributions of bar strengths (e_{bar}) in the B (Figs. 13a,c) and H bands (Figs. 13b,d). It is striking that only a very small proportion (7% in B ; 10% in H) of bars are very weak with $0.25 \leq e_{\text{bar}} \leq 0.40$, while the majority of bars (70% in B ; 71% in H) have moderate to high strengths, with $0.50 \leq e_{\text{bar}} \leq 0.75$. This point is further illustrated in Figure 14, which is a generalized plot of the fraction of disks with ‘strong’ and ‘weak’ bars. It shows how the fraction of spiral galaxies that host bars with strengths ($e_{\text{bar}} > e_1$) changes as we vary e_1 . As we increase e_1 from 0.35 to 0.45, 0.55, and 0.75, the deprojected bar fraction in the B -band falls from 42% to 39%, 34%, and 7%, respectively, while the bar fraction in the H -band falls from 59% to 47%, 30%, and 1%. The flattening of the curve around $e_1 \sim 0.45$ is due to the paucity of bars with $0.25 \leq e_{\text{bar}} \leq 0.40$, while the steep fall the curve for e_1 in the range 0.50–0.75 shows the preponderance of ‘strong’ bars. This has implications for theoretical models that address the robustness of bars, and we refer the reader to § 4.5 for a discussion. At first glance our results on bar strength may seem in contradiction with those of Buta et al. (2005). They conclude that 40% of the galaxies in the OSUBSGS H band have ‘weakly barred’ or unbarred states ($Q_b \leq 0.1$), whereas we find only 6% ‘weak’ ($0.25 \leq e_{\text{bar}} \leq 0.4$) bars in the H band after deprojection. However, it should be noted that Buta et al. (2005) do not impose a lower limit on bar strength Q_b , but instead group together unbarred and weakly barred galaxies. Taking this into account, their results on the fraction of weak and unbarred states is, in fact, consistent with what we find if we group together our fraction of unbarred galaxies (40%) and ‘weakly barred’ galaxies (6%).

How does the bar strength, as characterized by e_{bar} , compare with RC3 visual bar classes that are based on visual inspection of optical B images (de Vaucouleurs et al. 1991)? The three RC3 visual bar classes, ‘A’, ‘AB’, and ‘B’ denote ‘unbarred’, ‘weakly barred’, and ‘strongly barred’ disks, respectively. As shown in Figure 15, our quantitative characterization of bars (§ 3.3) in the B -band indicates that 7%, 34%, and 79%, respectively, of the sample galaxies with RC3 visual classes of ‘A’, ‘AB’, and ‘B’, host bars. In the H -band, the corresponding numbers are 18%, 64%, and 84%, respectively. Thus, a significant percentage of galaxies that are classified as unbarred in RC3 turn out to be barred and vice-versa. The mean bar strength e_{bar} is higher for RC3 visual class ‘B’ than for class ‘AB’, but the two classes have significant overlap in the range $e_{\text{bar}} \sim 0.5$ –0.7. Thus, RC3 bar types should be used with caution and may be misleading.

It is also noteworthy that Figure 13 shows no evidence for bimodality in the distribution of bar strength in the B or H bands, in agreement with Buta et al. (2005). Both our study and that of Buta et al. (2005) disagree with Whyte et al. (2002), who report a bimodal distribution of bar strengths. We suggest two possible reasons for this difference. Firstly, the Whyte et al. (2002) study suffers from smaller number statistics compared to the first two studies. The Buta et al. (2005) study applied the Q_b method

to H band images of 147 OSUBSGS galaxies, which is a sample comparable in size to our sample S3 of 169 OSUBSGS galaxies or our sample S4 of 137 moderately inclined OSUBSGS galaxies (Fig. 1). In contrast, the Whyte et al. (2002) study involved only 89 galaxies in the B band and 113 galaxies in the H band after the exclusion of inclined galaxies. From this, they were left with only 72 galaxies that had images in both the B and H bands, compared to 137 in our sample S4. Aside from number statistics, a second possible reason for the difference is that the ellipse fits were analyzed differently by Whyte et al. (2002) and our study. We inspected the overlays of the fitted ellipses on the galaxy images for all cases, and then applied stringent quantitative criteria to the *full radial profile* of (SB, e , and PA) when identifying bars (Fig. 1 and § 3). In particular, we required a smooth rise in e and a constant PA plateau along the bar, and a break between the bar and disk regions, before calling a feature a bar. In contrast, the Whyte et al. (2002) study did not analyze the full radial profile of (SB, e , and PA), but simply characterized a bar as being the innermost feature whose isophote has the highest ellipticity. It is thus possible that spurious features were misidentified as bars. This misidentification, along with the smaller number statistics, may have led to an artificial bimodality in bar strength in their study.

4.4. Bar fraction and strength as a function of Hubble type at $z \sim 0$

Figure 16 shows how the fraction of barred disks varies across different Hubble types in sample S4. The Hubble types are taken from RC3 and the bins represent S0, Sa/Sab, Sb/Sbc, Sc/Sd, and Sd/Sm. We find that the bar fraction in different Hubble types does not change significantly after deprojection, whether in the B (Fig. 16a vs. 16d) or H (Fig. 16b vs. 16e) band images. Furthermore, the H band bar fraction (Fig. 16e) remains $\sim 60\%$ across different Hubble types. Our quantitative result is consistent with the qualitative results of Eskridge et al. (2000), who also report a constant NIR bar fraction as a function of RC3 Hubble types, based on visual inspection. We also find no difference in the $B - V$ color or luminosity L_B in barred and unbarred galaxies. The large H -band bar fraction of $\sim 60\%$ across different Hubble types implies that bars are ubiquitous in spirals across the entire Hubble sequence. Further implications are discussed in § 4.5.

In the B band, we find that the bar fraction is lower with respect to the H band by $\sim 1.2\text{--}1.5$ in S0s to Scs, and by ~ 2.5 in Sds/Sm (Fig. 16c,f). This is consistent with higher obscuration in dusty, gas-rich late types. Eskridge et al. (2000) also find that the increase in bar fraction from the B to H band is most significant for late-type galaxies.

How does the bar strength vary as a function of Hubble type? In the H band, the bar strength e_{bar} lies in the range 0.35–0.80, and shows no systematic variation across Hubble types S0, Sa/Sab, Sb/Sbc, Sc/Sd, and Sd/Sm, either before (Fig. 17a) or after (Fig. 17b) deprojection. In particular, there is no evidence that bars have lower strength/ellipticities toward earlier Hubble types, and we return to this point in § 4.5.

4.5. Constraints on the robustness and evolution of bars

The robustness and lifetime of bars define some of the most fundamental issues in the evolution of bars, their impact on their host galaxies (§ 1) and the assembly of the Hubble sequence. In general terms, the evolution of a bar depends on the exchange of angular momentum between the stars in the bar and the surrounding dark matter halo and baryonic (gas and stars) components. Important factors influencing the bar include the triaxiality of the dark matter (DM) halo in which it lies (e.g., Berentzen, Shlosman, & Jogee 2006); the central mass concentrations (CMC) present in the inner few hundred pc (e.g., Shen & Sellwood 2004; Athanassoula et al. 2005; Hozumi & Hernquist 2005; Martinez-Valpuesta et al. 2006; Debattista et al. 2006); and the distribution and amount of gas in the disk (e.g., Shlosman & Noguchi 1993; Bournaud et al. 2002, 2005; Debattista et al. 2006). In this section, we compare our empirical results to different simulations in order to constrain theoretical scenarios. We note, however, that most simulations do not yet fully incorporate the effects of star formation and feedback, which can impact the evolution of the disk in important ways.

Simulations by Berentzen, Shlosman, & Jogee (2006) find that bars embedded in triaxial dark matter halos can only survive if the halo triaxiality is very diluted, with a maximum equatorial axial ratio b/a of ~ 0.7 in density, and ~ 0.9 in potential. For higher triaxialities, the interaction between the bar and dark matter halo induces chaotic orbits and destroys the bar. In the present paper, our findings that the majority (60%) of spirals are barred in the infrared (§ 4.1), and that these bars have primarily moderate to high strengths ($0.50 \leq e_{\text{bar}} \leq 0.80$; § 4.3) suggest that DM halos of most present-day spirals are close to axisymmetric, with a maximum equatorial axial ratio of ~ 0.9 in potential. These results are consistent with Kazantzidis et al. (2004), who find that in the very early stages of disk formation, the settling of the dissipative baryonic component within a triaxial halo strongly dilutes the triaxiality to such values.

The CMC typically refers to the mass present within the inner 100 or few hundred pc. A large or more centrally concentrated CMC can weaken a bar amplitude by changing the orbital structure of a barred potential and inducing chaotic orbits. Most simulations (e.g., Athanassoula et al. 2005; Shen & Sellwood 2004; Martinez-Valpuesta et al. 2006; Debattista et al. 2006) find that in order to produce any significant effect on the bar strength, the ratio $X_{\text{CMC}} \sim (M_{\text{CMC}}/M_{\text{disk}})$, where M_{CMC} is the mass of the CMC in the inner few hundred pc, and M_{disk} is the disk mass, must be very large, at least 10%. However, in contrast, simulations of Hozumi & Hernquist (2005) seem to destroy bars using much smaller CMCs.

What do our results suggest? We first note that in present-day galaxies, the components that make up the CMC in the inner few hundred pc and contribute to X_{CMC} , consist of supermassive black holes (SMBHs), central dense stellar clusters, gaseous concentrations, and the inner parts of bulges. We found that the majority ($\sim 71\text{--}80\%$) of bars have moderate to high strengths ($0.50 \leq e_{\text{bar}} \leq 0.80$). We also found that the bar fraction ($\sim 60\%$) and mean bar strength ($e_{\text{bar}} \sim 0.5$) is relatively constant across the Hubble sequence (§ 4.4), although the latter encompasses a wide range of gas mass

fractions, CMC masses, and CMC components, such as SMBHs, gas concentrations, and bulges. These results suggest that most bars in present-day galaxies are relatively robust against the range in CMCs and other host galaxy properties present along the Hubble sequence. Our results on CMCs are in agreement with those simulations that support robust bars.

Gas can affect the formation and evolution of a bar in different ways, depending on its distribution and clumpiness. In the case of an unbarred disk, the accretion of cold gas makes the disk more massive, dynamically colder, and therefore more bar unstable (e.g., Bournaud et al. 2002). However, in the case of very gas-rich disks, the gas can become clumpy, and the effect of dynamical friction on massive gas clumps at low radii can heat the disk and prevent it from forming the bar (e.g., Shlosman & Noguchi 1993). In the case of a disk that is already barred, the bar exerts gravitational torques that drive gas located outside the corotation resonance (CR) outward, and drives gas located between the CR and inner Lindblad resonance (ILR) inward. The inflow of gas into the inner kpc can destroy bars in several simulations, but there is a lot of debate as to whether the conditions for this destruction are met in real galaxies. For instance, some simulations (e.g., Debattista et al. 2006), can only destroy the bar when there are large gas inflows that build a very massive soft CMC, of order 20% of the mass of the total baryonic (gas and stars) disk. These type of CMCs are not common in present-day galaxies and the simulations would suggest, therefore, that most bars in present-day galaxies are robust and remain strong even in the presence of bar-driven gas inflows. Furthermore, the simulations also suggest that gas which sinks into the center can become bar supporting if it forms stars. On the other hand, other simulations of bar-driven gas inflow (e.g., Bournaud et al. 2005) can destroy a bar in a disk with a gas mass fraction (GMF) that is as low as 5% to 7%. Here, the GMF is defined as the ratio of gas mass to the total mass of the stellar disk. A GMF of order 5% is easily met in present-day galaxies and this class of simulations would suggest, therefore, that strong bars in present-day galaxies are easily destroyed by bar-driven gas inflow (Bournaud et al. 2005). At least part of the reason why the simulation results are so different might lie in the way the DM halo is modeled and the assumed ratio of DM halo mass to disk mass. The DM halo is live and dominates over the disk mass in Debattista et al. (2006), while it is rigid and less massive than the disk in Bournaud et al. (2005).

What do our observational results suggest? We found that at $z \sim 0$, only a small fraction ($\sim 7\%-10\%$) of bars are very weak ($0.25 \leq e_{\text{bar}} \leq 0.40$), while the majority ($\sim 71\%-80\%$) of bars have moderate to high strengths ($0.50 \leq e_{\text{bar}} \leq 0.80$). We also do not see any sign of bimodality in bar strength. Finally, we found that the bar fraction ($\sim 60\%$) and mean bar strength ($e_{\text{bar}} \sim 0.5$) is relatively constant across Hubble types (§ 4.4), despite the wide variation in GMFs. Our results are easily reconciled with scenarios where bars in present-day moderately gas-rich galaxies remain strong under the effect of bar-driven gas inflows (e.g., Debattista et al. 2006). However, our empirical results do not necessarily rule out models where the bars are easily destroyed by bar-driven gas inflow. They

do, however, imply that if such an easy destruction occurs, then there must be a very efficient mechanism to regenerate the bars on a short timescale. Block et al. (2002) and Bournaud et al. (2002) have suggested that the external accretion of large amounts of cold gas may represent such a mechanism.

4.6. Comparison of optical properties of bars at $z \sim 0$ and at $z \sim 0.2\text{--}1.0$

One motivation for our study is to provide a rest-frame optical $z \sim 0$ point for bars based on ellipse fits, which we can compare with studies of intermediate redshift bars (J04; E04; Z05) that use the same or similar methods. In particular, we have applied to the $z \sim 0$ OSUBSGS galaxies the same procedure of ellipse fits (§ 3.1) and the same criteria for bar characterization (§ 3.3) that J04 applied to galaxies at intermediate redshifts $z \sim 0.2\text{--}1.0$ (corresponding to lookback time $\sim 3\text{--}8$ Gyr).

The study of intermediate redshift bars by J04 was based on high resolution *HST* ACS two-band optical images from the GEMS (Rix et al. 2004) survey, along with accurate redshifts from the COMBO-17 survey (Wolf et al. 2004). The characterization of bar fractions was restricted to $z \sim 0.2\text{--}1.0$ bright spirals ($M_V \leq -19.3$) that host bars with moderate-to-high strength ($e_{\text{bar}} \geq 0.4$) for the following reasons. In order to ensure that the sample of spiral galaxies is fairly complete out to $z \sim 0.9$, an absolute magnitude cutoff of $M_V \leq -19.3$ had to be applied. Furthermore, the study only considered bars with strength/ellipticity $e_{\text{bar}} \geq 0.4$ because at intermediate redshifts, it becomes difficult to unambiguously identify and characterize bars with lower ellipticities. It is also to be noted that at $z > 0.5$, where $1''$ corresponds to scales > 6.2 kpc, the study could not efficiently resolve very small bars with semi-major axes $a < 1.5$ kpc, in agreement with Lisker et al. (2006). However, such small bars are considered as nuclear bars rather than large-scale bars, and are therefore irrelevant for the study. With these criteria, J04 find that at *rest-frame optical* wavelengths, the fraction (f_{GEMS}) of bright ($M_V \leq -19.3$) spirals, which host large-scale ($a_{\text{bar}} \geq 1.5$ kpc) bars of moderate-to-high strengths (ellipticities) $e_{\text{bar}} \geq 0.4$, remains at $\sim 30 \pm 6\%$ over $z = 0.2\text{--}1.0$. A constant and similar optical bar fraction out to intermediate redshifts is also reported by E04 and Z05.

We investigate what is the corresponding optical bar fraction at $z \sim 0$ from OSUBSGS if we impose similar criteria. We use observed bar properties prior to deprojection from OSUBSGS because no deprojection was applied to intermediate redshift studies of J04, E04 and Z05. We find that in the *B*-band, the fraction of bright ($M_V \leq -19.3$) spirals that host large-scale bars ($a_{\text{bar}} \geq 1.5$ kpc) with bar strength $e_{\text{bar}} \geq 0.4$ is $f_{\text{OSU}} \sim 35 \pm 6\%$ at $z \sim 0$, based on OSUBSGS. These cuts in magnitudes, bar ellipticity, or bar semi-major axis turn out not to be particularly severe because few disks in OSUBSGS are fainter than $M_V \sim -19.3$ (see Fig. 3b), and very few bars have $e_{\text{bar}} < 0.4$ (see Fig. 13 and 14) or $a_{\text{bar}} < 1.5$ kpc (see Fig. 10).

The fact that the optical bar fraction at $z \sim 0.2\text{--}1.0$ from GEMS ($f_{\text{GEMS}} \sim 30 \pm 6\%$; J04) is comparable to that at $z \sim 0$ from OSUBSGS ($f_{\text{OSU}} \sim 35 \pm 6\%$) rules

out cosmogonies where the optical bar fraction in the Universe declines strongly with redshift. Such models would yield $f_{\text{GEMS}} \ll f_{\text{OSU}}$ because the observed bar fraction would be lowered both by intrinsic model trends, and by systematic effects at intermediate redshifts, such as cosmological dimming, the loss of spatial resolution, and lower signal-to-noise.

However, our finding that f_{GEMS} is comparable to f_{OSU} allows for models where the optical bar fraction is either constant, or rises with redshift. In the latter class of models, one can arrive at comparable values of f_{GEMS} and f_{OSU} only if the intrinsic increase in bar fraction with redshift produced by the model is compensated for by the ‘loss’ of bars due to systematic effects, such as cosmological dimming, and low signal-to-noise. In a forthcoming paper (Paper II), we will assess the impact of such redshift-dependent systematic effects by artificially redshifting the OSUBSGS B band sample to $z \sim 1$, and repeating the bar characterizations. This will enable us to distinguish between the two classes of models.

5. SUMMARY AND CONCLUSIONS

In this study, we characterize the frequency and structural properties of bars in the local Universe at optical and NIR wavelengths by ellipse-fitting the B and H images of 180 spirals in the OSU Bright Spiral Galaxy Survey (Eskridge et al. 2002), and applying quantitative criteria in order to identify and characterize bars. We determine the inclination of the outer disk and exclude highly inclined ($i > 60^\circ$) galaxies to derive a sample S4 of 137 moderately inclined spirals. For this sample, we derive bar properties both before and after deprojection to face-on. Our study complements existing work on OSUBSGS based on Fourier amplitudes (Block et al. 2002; Buta et al. 2005) and visual classification (Eskridge et al. 2000), and it can be compared with studies (J04; E04; Z05) of intermediate redshift ($z \sim 0.2\text{--}1.0$) bars employing the same ellipse-fitting methodology. Our results are summarized below.

(1) The optical and NIR bar fraction at $z \sim 0$: We find a deprojected bar fraction of 60% in the H -band, confirming the preponderance of bars among spirals in the local Universe. The bar fraction is lower (44%) in the B -band images, which likely miss bars obscured by dust and star formation. We note that deprojection does not make any significant changes to the global B and H band bar fractions, which are 42% and 58% before deprojection, and change by only a factor of 1.04 and 1.03, respectively, after deprojection. This is encouraging for large studies of bars at intermediate redshift (e.g., J04, E04, Z05), where deprojection is not usually performed.

(2) Sizes of bars and disks at $z \sim 0$: The sizes or semi-major axes a_{bar} of bars in the local Universe lie in the range ~ 1 to 14 kpc, with the majority of bars (72% in B and 76% in H) having $a_{\text{bar}} \leq 5$ kpc. Bar and disk sizes are correlated with an average slope of ~ 0.9 , albeit with a large scatter of several kpc in bar size at a given disk size. The ratio (a_{bar}/R_{25}) lies primarily in the range 0.2 to 0.4. The correlation between bar and disk sizes, and the narrow range in a_{bar}/R_{25} suggest that the growths of the bar and disk may be intimately tied. The fact that (a_{bar}/R_{25}) is generally well below 1.0 suggests that the CR of disk galaxies lies well inside their R_{25} radius, assuming that

bars end near the CR.

(3) Distribution of bar strengths at $z \sim 0$: In this study, we use the bar ellipticity e_{bar} as a measure of the bar strength. Only a very small proportion (7% in B ; 10% in H) of bars are very weak ($0.25 \leq e_{\text{bar}} \leq 0.40$), while the majority of bars (70% in B ; 71% in H) seem to have moderate to high strengths ($0.50 \leq e_{\text{bar}} \leq 0.75$). We find no evidence for bimodality in the distribution of bar strength in the B or H bands, in agreement with Buta et al. (2005). We compare the bar strength characterized by e_{bar} with RC3 visual bar classes. Of the galaxies with RC3 visual classes of ‘A’, ‘AB’, and ‘B’, we find that 7%, 34%, and 79% are barred in the B -band and 18%, 64%, and 84% are barred in the H -band. Thus, a significant percentage of galaxies that are classified as unbarred in RC3 turn out to be barred and vice-versa. The mean bar strength e_{bar} is higher for RC3 visual class ‘B’ than for class ‘AB’, but the two classes have significant overlap in the range $e_{\text{bar}} \sim 0.5\text{--}0.7$. Thus, RC3 bar types should be used with caution and may be misleading.

(4) Bar fraction and strength as a function of Hubble type at $z \sim 0$: The bar fraction in the H band remains $\sim 60\%$ across different RC3 Hubble types from S0s to Sds/Sms. In the B band, the bar fraction is lower with respect to the H band by $\sim 1.2\text{--}1.5$ for Hubble types S0s to Scs, and by ~ 2.5 for Sds/Sms. This is consistent with the higher obscuration in dusty, gas-rich late types. The bar strength e_{bar} in the H band is primarily in the range 0.40–0.80 and shows no systematic variation across Hubble types.

(5) Constraints on the robustness of bars: We compare our observational results at $z \sim 0$ to simulations and set constraints of factors impacting the robustness of bars: (a) Our findings that the majority (60%) of spirals are barred in the infrared and that these bars have primarily moderate to high strengths ($0.50 \leq e_{\text{bar}} \leq 0.80$) suggest that DM halos of present-day spirals have at most a mild triaxiality, with a maximum equatorial axis ratio $b/a \sim 0.9$ in the potential. (b) We also found that at $z \sim 0$, only a small fraction ($\sim 7\%\text{--}10\%$) of bars are very weak ($0.25 \leq e_{\text{bar}} \leq 0.40$), while the majority ($\sim 71\%\text{--}80\%$) of bars have moderate to high strengths ($0.50 \leq e_{\text{bar}} \leq 0.80$). There is no sign of bimodality in bar strength. Finally, we found that the bar fraction ($\sim 60\%$) and mean bar strength ($e_{\text{bar}} \sim 0.5$) is relatively constant across Hubble types (§ 4.4). Taken together, these results suggest that most bars in $z \sim 0$ galaxies are relatively robust against the range in gas mass fractions, CMC components (SMBHs, gas concentrations, and bulges) and other galaxy properties along the Hubble sequence. Our results are easily reconciled with scenarios where bars in present-day moderately gas-rich galaxies remain strong under the effect of bar-driven gas inflows. However, our empirical results do not rule out models where the bars are easily destroyed by bar-driven gas inflow. They do, however, imply that if such an easy destruction occurs, then there must be a very efficient mechanism to regenerate the bars on a short timescale.

(6) Comparison of optical properties of bars at $z \sim 0$ and at intermediate redshifts: Earlier studies (J04) of bars at $z \sim 0.2\text{--}1.0$ or lookback times of 3–8 Gyr report a bar fraction, $f_{\text{GEMS}} \sim 30 \pm 6\%$, in the rest-frame optical for

bright ($M_V < -19.3$) disks that host large-scale ($a_{\text{bar}} \geq 1.5$ kpc) bars with moderate-to-high strengths ($e_{\text{bar}} \geq 0.4$). For these type of systems in OSUBSGS, the corresponding B band bar fraction at $z \sim 0$ has a comparable value of $f_{\text{OSU}} \sim 35 \pm 6\%$. The result that f_{GEMS} is comparable to f_{OSU} rules out cosmogonies where the optical bar fraction in the Universe declines strongly with redshift. It allows for models where the optical bar fraction is either constant, or rises with redshift.

S.J. and I.M. acknowledge support from NSF grant AST-0607748, NASA LTSA grant NAG5-13063, as well as

HST grants G0-1048 and G0-10395 from STScI, which is operated by AURA, Inc., for NASA, under NAS5-26555. The Ohio State University Bright Spiral Galaxy Survey, was funded by grants AST-9217716 and AST-9617006 from the United States National Science Foundation, with additional support from the Ohio State University. We thank Pat Shopbell, Peter Teuben, and Stuart Vogel for their assistance with the Zodiac and MIRIAD packages; Seppo Laine for sharing his deprojection code from Laine et al (2002); and James Davies for help with IRAF and IGI visualization routines.

REFERENCES

Aguerri, J. A. L., Debattista, V. P., & Corsini, E. M. 2003, MNRAS, 338, 465

Athanassoula, E. 1992a, MNRAS, 259, 328

Athanassoula, E. 1992b, MNRAS, 259, 345

Athanassoula, E. 2002, ApJL, 569, 83

Athanassoula, E., & Misiriotis, A. 2002, MNRAS, 330, 35

Athanassoula, E. 2003, MNRAS, 341, 1179

Athanassoula, E. 2005, MNRAS, 358, 1477

Athanassoula, E., Lambert, J. C., & Dehnen, W. 2005, MNRAS, 363, 496

Barazza, F., Jogee, S., Marinova, I. 2006 (in prep)

Berentzen, I., Shlosman, I., & Jogee, S. 2006, ApJ, 637, 582

Block, D. L., Bertin, G., Stockton, A., Grosbol, P., Moorwood, A. F. M., & Peletier, R. F. 1994, A&A, 288, 365

Block, D. L., Bournaud, F., Combes, F., Puerari, I., & Buta, R. 2002, A&A, 394, L35

Bournaud, F., & Combes, F. 2002, A&A, 392, 83

Bournaud, F., Combes, F., & Semelin, B. 2005, MNRAS, 364, L18

Bureau, M., & Athanassoula, E. 2005, ApJ, 626, 159

Buta, R., Vasylyev, S., Salo, H., & Laurikainen, E. 2005, AJ, 130, 506

Combes, F., & Sanders, R. H. 1981, A&A, 96, 164

Combes, F., Debbasch, F., Friedli, D., & Pfenniger, D. 1990, A&A, 233, 82

Debattista, V. P., & Sellwood, J. A. 1998, ApJL, 493, L5

Debattista, V. P., & Sellwood, J. A. 2000, ApJ, 543, 704

Debattista, V. P., Corsini, E. M., & Aguerri, J. A. L. 2002, MNRAS, 332, 65

Debattista, V. P., Mayer, L., Carollo, C. M., Moore, B., Wadsley, J., & Quinn, T. 2006, ApJ, 645, 209

de Vaucouleurs, G., de Vaucouleurs, A., Corwin Jr., H. G., Buta, R. J., Paturel, G., & Fouque, P. 1991, Third Reference Catalogue of Bright Galaxies (New York: Springer) (RC3)

Elmegreen, B. G., & Elmegreen, D. M. 1985, ApJ, 288, 438

Elmegreen, B. G., Elmegreen, D. M., Chromeley, F. R., Hasselbacher, D. A., & Bissell, B. A. 1996, AJ, 111, 2233

Elmegreen, B. G., Elmegreen, D. M., & Hirst, A. C. 2004, ApJ, 612, 191 (E04)

Erwin, P. 2005, MNRAS, 364, 283

Eskridge, P. B., et al. 2000, AJ, 119, 536

Eskridge, P. B., et al. 2002, ApJS, 143, 73

Hozumi, S., & Hernquist, L. 2005, PASJ, 57, 719

Hunt, L. K., & Malkan, M. A. 1999, ApJ, 516, 660

Jogee, S. 1999, Ph.D. thesis, Yale University

Jogee, S., Kenney, J. D. P., & Smith, B. J. 1999, ApJ, 526, 665

Jogee, S., Knapen, J. H., Laine, S., Shlosman, I., Scoville, N. Z., & Englmaier, P. 2002a, ApJL, 570, L55

Jogee, S., Shlosman, I., Laine, S., Englmaier, P., Knapen, J. H., Scoville, N., & Wilson, C. D. 2002b, ApJ, 575, 156

Jogee, S., Barazza, F., Rix, H.-W., Shlosman, I. et al. 2004a, ApJL, 615, L105 (J04)

Jogee, S., Scoville, N., & Kenney, J. D. P. 2005, ApJ, 630, 837

Jogee, S., 2006, Lecture Notes in Physics, Vol. 693, "AGN Physics on All Scales", Eds. D. Alloin, R. Johnson, & P. Lira (Springer: Berlin Heidelberg New York), Vol. 93, Chapter 6, p 143 (astro-ph/0408383).

Kazantzidis, S., Kravtsov, A. V., Zentner, A. R., Allgood, B., Nagai, D., & Moore, B. 2004, ApJL, 611, L73

Knapen, J. H., Beckman, J. E., Heller, C. H., Shlosman, I., & De Jong, R. S. 1995, ApJ, 454, 623

Knapen, J. H., Shlosman, I., & Peletier, R. F. 2000, ApJ, 529, 93

Kormendy, J. 1993, in Proceedings of IAU Symposium 153, Galactic bulges, ed. H. DeJonghe and H. J. Habing, (Dordrecht: Kluwer), 209

Kormendy, J., & Kennicutt, R. C. 2004, ARAA, 42, 603

Laine, S., Shlosman, I., Knapen, J. H., & Peletier, R. F. 2002, ApJ, 567, 97

Laurikainen, E., Salo, H., & Rautiainen, P. 2002, MNRAS, 331, 880

Laurikainen, E., Salo, H., & Buta, R. 2004, ApJ, 607, 103

Lisker, T., Debattista, V. P., Ferreras, I., & Erwin, P. 2006, MNRAS, 370, 477

Martinez-Valpuesta, I., Shlosman, I., & Heller, C. 2006, ApJ, 637, 214

Menendez-Delmestre, K. et al., 2004, in "Penetrating Bars Through Masks of Cosmic Dust: The Hubble Tuning Fork Strikes a New Note", Eds. D. Block, I. Puerari, K. Freeman, R. Groess, & E. Block (Springer), pp. 787-8

Merrfield, M. R., & Kuijken, K. 1995, MNRAS, 274, 933

Mihos, J. C., & Hernquist, L. 1996, ApJ, 464, 641

Mulchaey, J. S., & Regan, M. W. 1997, ApJL, 482, L135

Noguchi, M. 1988, A&A, 203, 259

Pfenniger, D., & Norman, C. 1990, ApJ, 363, 391

Rix, H.-W., et al. 2004, ApJS, 152, 163

Regan, M. W., Vogel, S. N., & Teuben, P. J. 1997, ApJ, 482, L143

Schwarz, M. P. 1981, ApJ, 5247, 77

Shen, J., & Sellwood, J. A. 2004, ApJ, 604, 614

Sheth, K., Regan, M. W., Scoville, N. Z., & Strubbe, L. E. 2003, ApJL, 592, L13

Shlosman, I., Frank, J., & Begelman, M. C. 1989, Nature, 338, 45

Shlosman, I., Begelman, M. C., & Frank, J. 1990, Nature, 345, 679

Shlosman, I., & Noguchi, M. 1993, ApJ, 414, 474

Tully, R. B. 1988, Cambridge and New York, Cambridge University Press, 221 p., (NPG)

Weinberg, M. D. 1985, MNRAS, 213, 451

Whyte, L. F., Abraham, R. G., Merrifield, M. R., Eskridge, P. B., Frogel, J. A., & Pogge, R. W. 2002, MNRAS, 336, 1281

Wolf, C., et al. 2004, A&A, 421, 913

Wozniak, H., Friedli, D., Martinet, L., Martin, P., & Bratschi, P. 1995, A&A Suppl., 111, 115

Zheng, X. Z., Hammer, F., Flores, H., Assémat, F., & Rawat, A. 2005, A&A, 435, 507 (Z05)

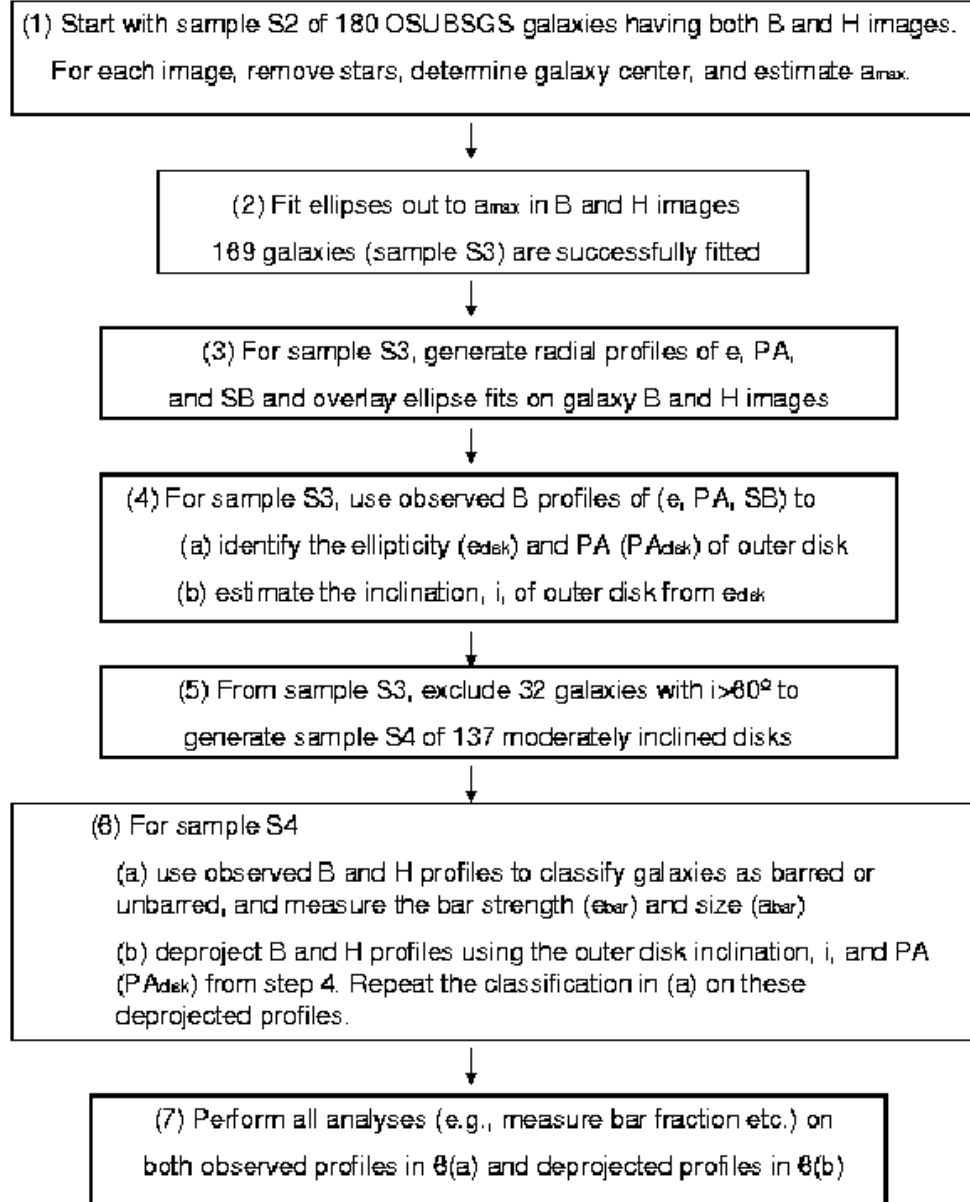


FIG. 1.— **Analysis steps for characterizing bars and disks at $z \sim 0$ from OSUBSGS:** Our procedure of characterizing bars and disks in OSUBSGS galaxies via ellipse fits is schematically illustrated in this figure and described in detail in § 3.1–3.4. For the B and H band images of the 180 galaxies in sample $S2$, we remove stars, find an accurate center, and determine the maximum semi-major axis of the galaxy, a_{\max} , where the galaxy isophotes reach the sky level. We fit ellipses out to a_{\max} to the B and H images of each galaxy, generate radial profiles of e , PA, and SB, and overlay the ellipses on the galaxy image for inspection. Successful fits are found in both bands for 169 galaxies (sample $S3$). For sample $S3$, we use the B band radial profiles to characterize the inclination i and PA of the outer disk. We exclude 32 galaxies with $i > 60^\circ$ to generate sample $S4$ of 137 moderately inclined galaxies. For sample $S4$, we deproject the B and H radial profiles using the outer disk i and PA, and use the deprojected profiles to characterize the properties of barred and unbarred disks. For completeness, we also perform this characterization on the the observed profiles before deprojection.

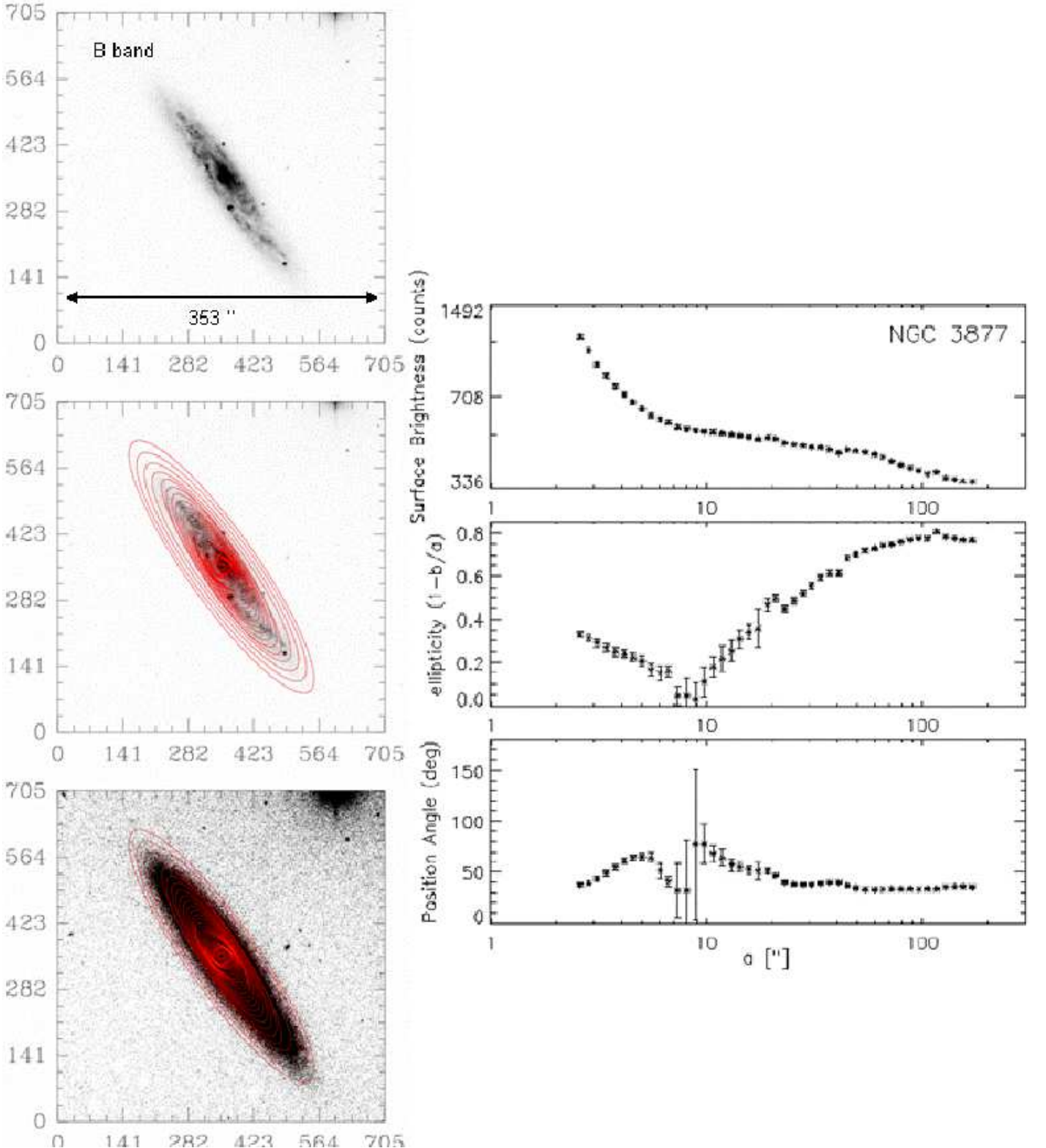


FIG. 2.— **Ellipse fits to the B band image of an inclined ($i > 60^\circ$) galaxy:** The left panel made of 3 images shows the ellipses fitted to the B band image of NGC 3877. The top image shows only the galaxy. The scale is shown on the top image in arcseconds, where $1'' = 86$ pc. The middle and bottom images show the ellipses overlaid on the galaxy, with greyscale stretches chosen to emphasize the inner (middle image) and outer (bottom image) regions of the galaxy. Note that ellipses are fitted out to the sky level in the image. The right panel shows the radial profiles of surface brightness (SB), ellipticity (e), and position angle (PA) versus semi-major axis (a) derived from the ellipse fits. The profiles show evidence for some structure in the inner regions, but at $a > 100''$, the e settles to a high value of 0.8, while the PA also settles to a constant value. This is the signature of an inclined disk with $i > 60^\circ$.

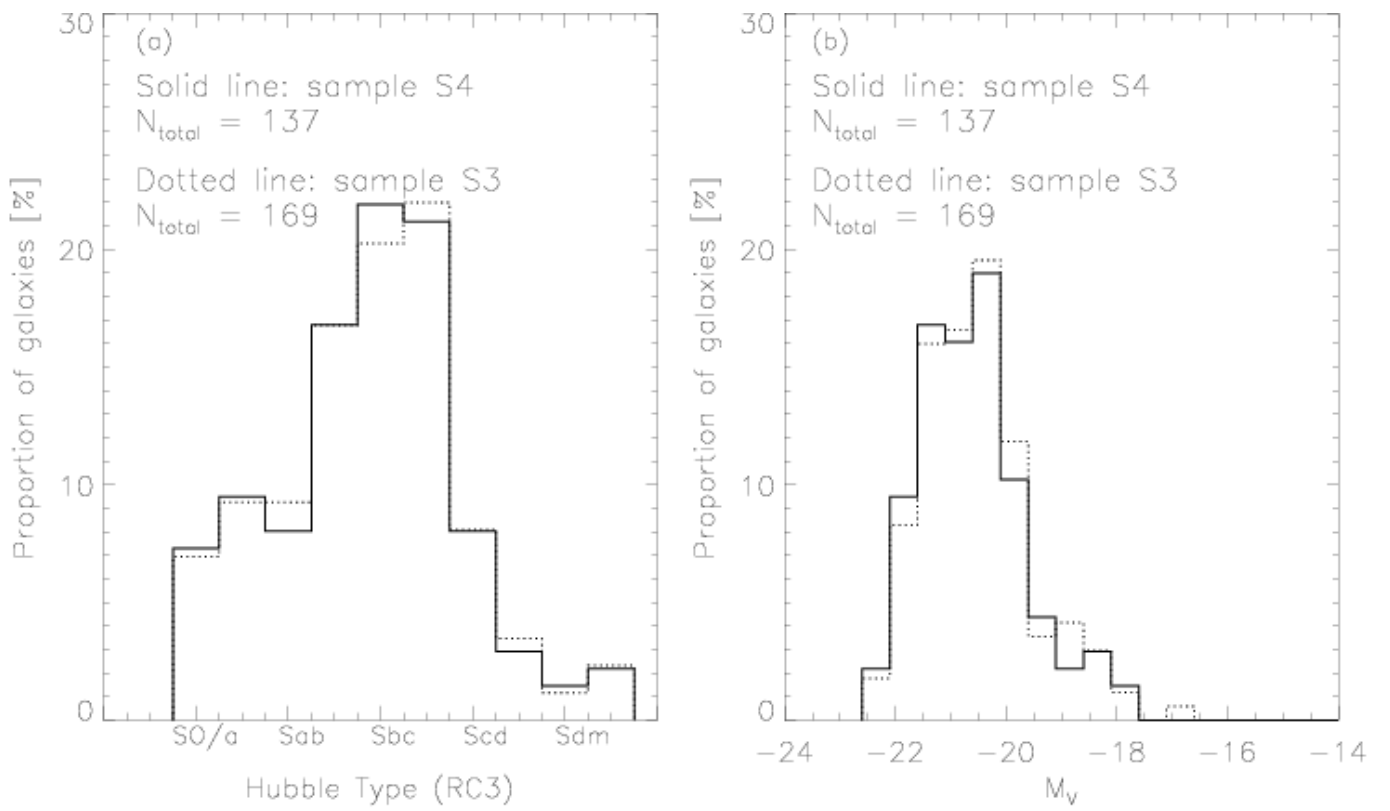


FIG. 3.— **Distribution of Hubble types and absolute magnitudes:** Left: The distributions of RC3 Hubble types are shown for the sample S4 (solid line) of 169 galaxies that include inclined systems, and for the sample S3 (dotted line) produced by excluding 32 galaxies with high inclination ($i > 60^\circ$). This exclusion does not significantly affect the Hubble type distribution of the sample. Right: The distributions of absolute V band magnitudes for sample S3 (solid line) and S4 (dotted line) are similar as well.

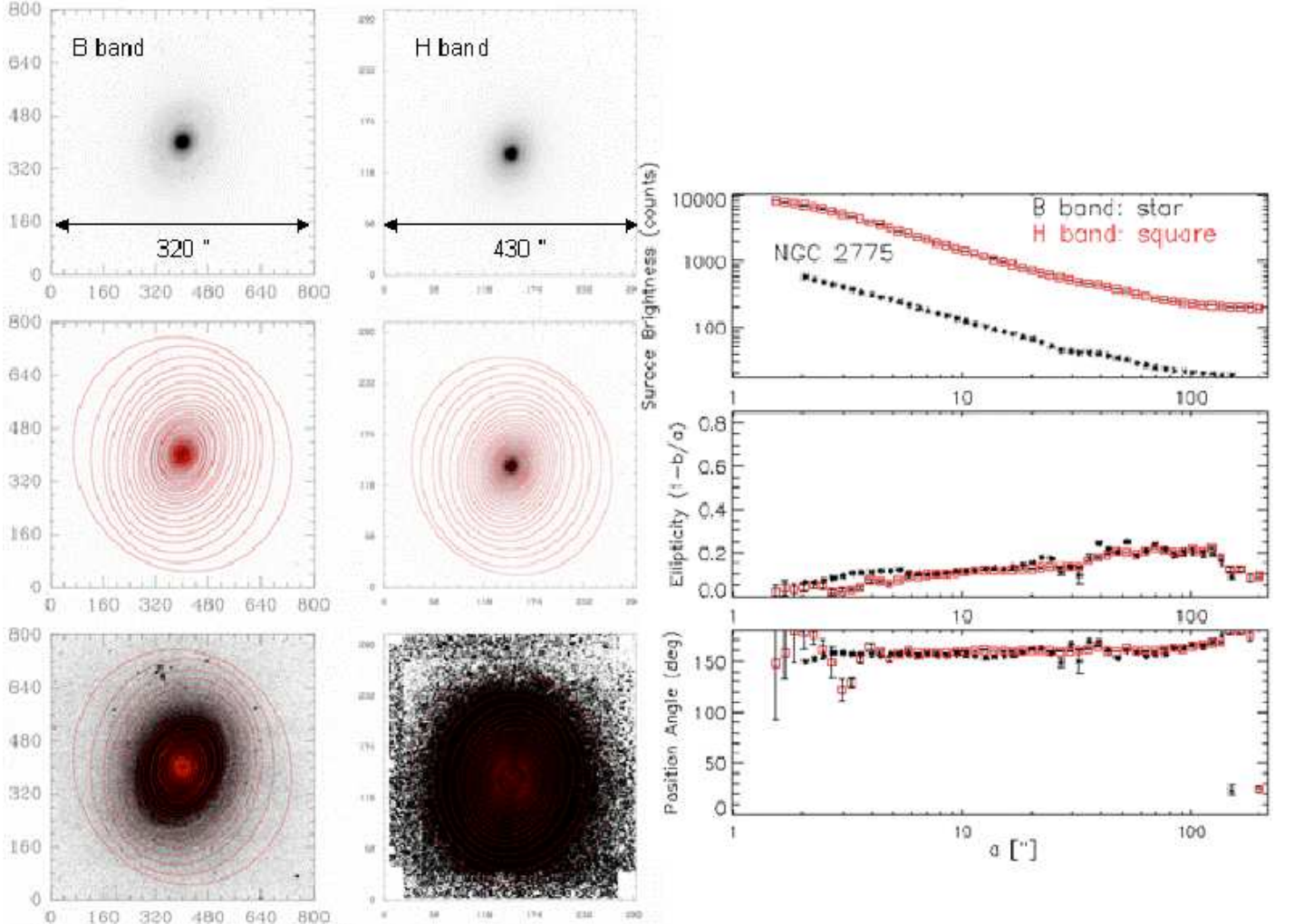


FIG. 4.— **Example of ellipse fits for the unbarred galaxy NGC 2775:** Left and middle panels: They show the ellipse-fits overlaid on the B and H band images of the unbarred galaxy NGC 2775. The scales of the B and H images are shown in the top image panels for each band. $1''$ corresponds to 86 pc at the galaxy distance of 17 Mpc. Within each panel, there are 3 images with different greyscale stretches that are chosen to emphasize the inner (middle image) and outer (bottom image) regions of the galaxy. Note that ellipses are fitted out to the sky level in the image. Right panel: This shows the radial profiles of (SB, e , and PA) for the B (stars) and H (squares) bands, derived from the ellipse fits prior to deprojection. The profiles do not show any characteristic bar signatures, such as a smooth rise in e to a maximum above 0.25, concurrent with a PA plateau. The e remains below 0.25 across the galaxy. There is no signature of large-scale structure, such as spiral arms or a bar.

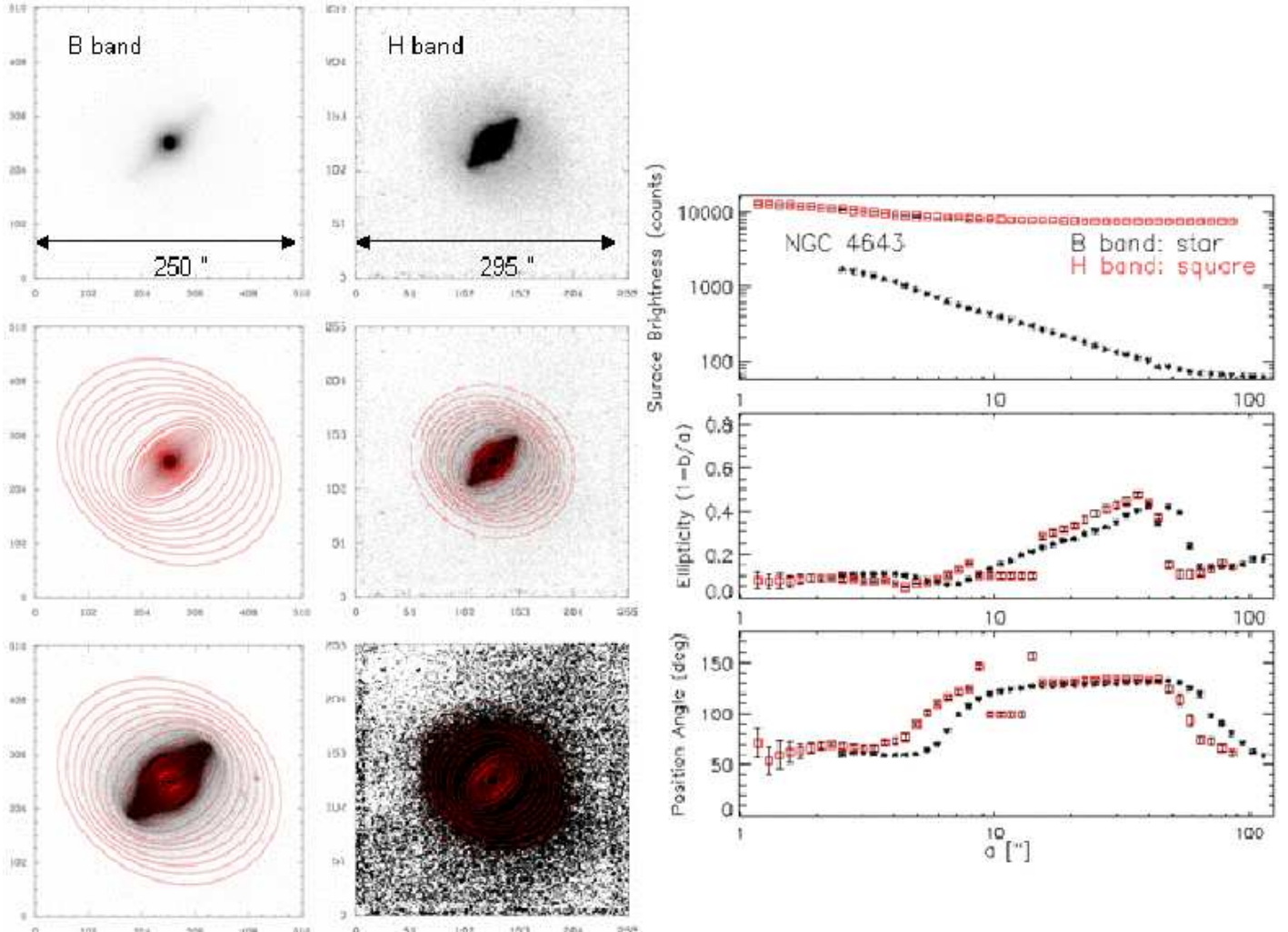


FIG. 5.— **Example of ellipse fits for the barred galaxy NGC 4643:** Left and middle panels: They show the ellipse-fits overlaid on the B and H band images of the barred galaxy NGC 4643. The scales of the B and H images are shown in the top image panels for each band. $1''$ corresponds to 130 pc at the galaxy distance of 26 Mpc. Within each panel, there are 3 images with different greyscale stretches that are chosen to emphasize the inner (middle image) and outer (bottom image) regions of the galaxy. Note that ellipses are fitted out to the sky level in the image. Right panel: This shows the radial profiles of (SB, e , and PA) for the B (stars) and H (squares) bands, derived from the ellipse fits and prior to deprojection. The profiles show a clear bar signature. Between $15''$ and $40''$, the e rises smoothly to a global maximum of 0.5, while the PA remains roughly constant. The e then drops to ~ 0.1 , and the PA changes at the transition from the bar to the disk region.

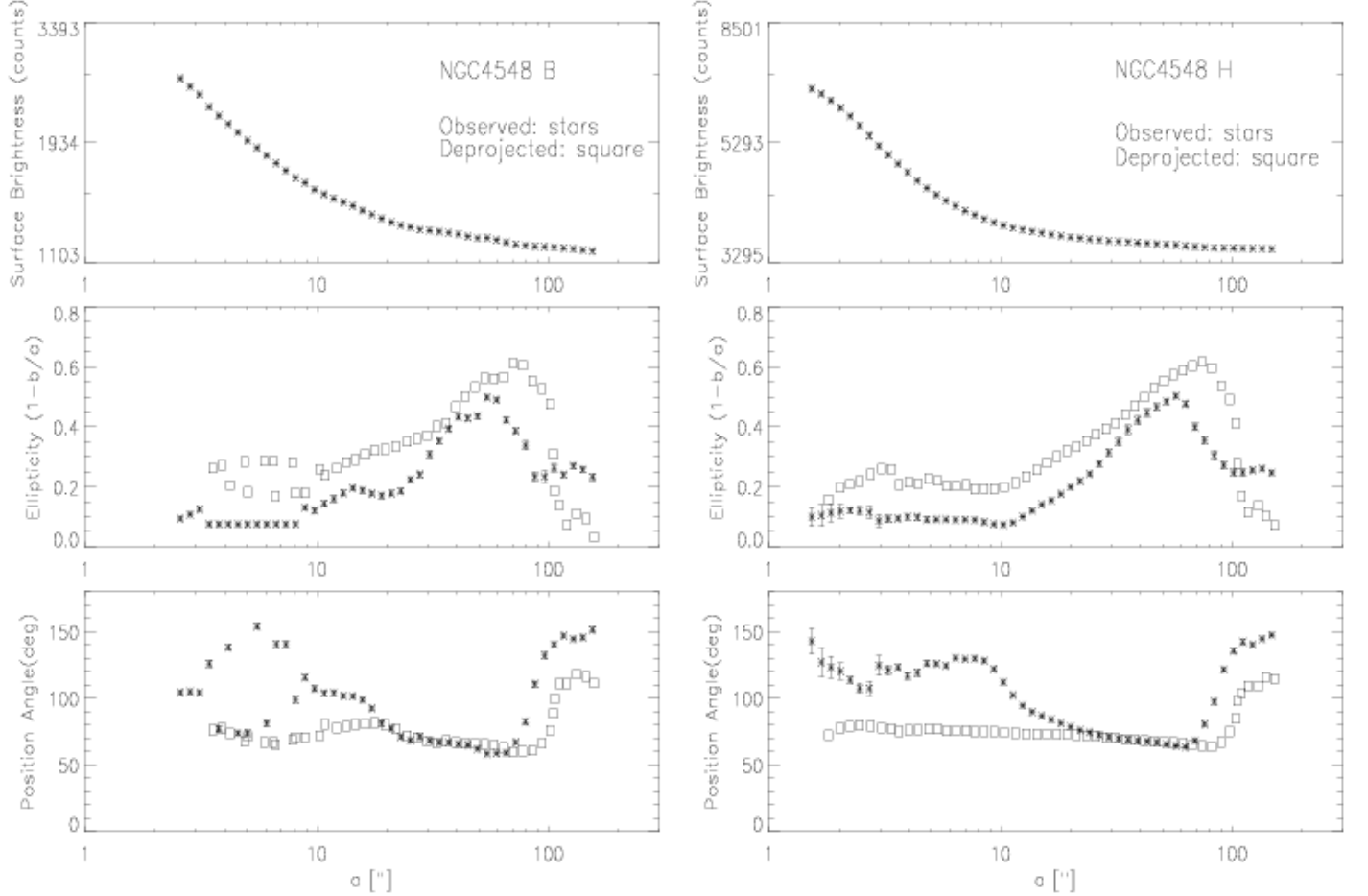


FIG. 6.— **Example of observed and deprojected radial profiles for NGC 4548:** For galaxies in sample S4, we use the inclination i and the PA of the outer disk (from § 3.2) to analytically deproject the observed H and B band radial profiles of (e, PA) to face-on. The case for NGC 4548 is illustrated here. The left panel shows the observed (stars) and deprojected (squares) radial profiles in the B band. The right panel shows the observed and deprojected radial profiles in the H band. After deprojection, as expected, the outer disk e is nearly zero in the B band. Note also that the bar size is slightly different and the bar appears somewhat stronger in both bands after deprojection.

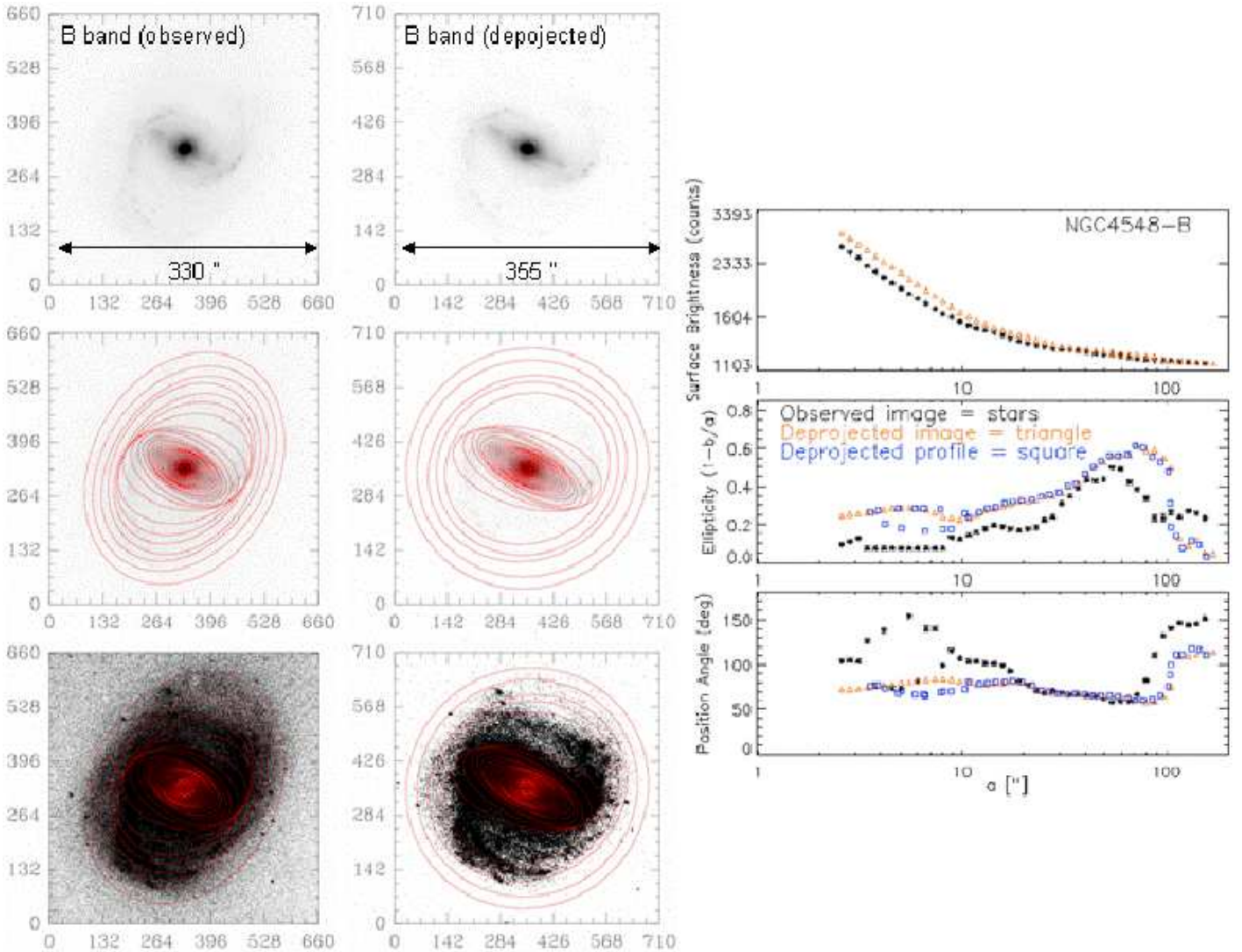


FIG. 7.— **Comparison of the face-on radial profile generated via two different methods:** For the B band image of NGC 4548, this figure compares the face-on radial profiles of e and PA generated via two different methods. In the first method, ellipses are fitted to the observed image (left panel) to generate the observed radial profile (plotted as stars in the right panel), which is then analytically deprojected to produce the face-on profile (plotted as squares in the right panel). In the second method, the observed image is deprojected with MIRIAD and the resulting deprojected image (middle panel) is fitted with ellipses to generate the second face-on profile (plotted as triangles in the right panel). Note the good agreement between the squares and triangles.

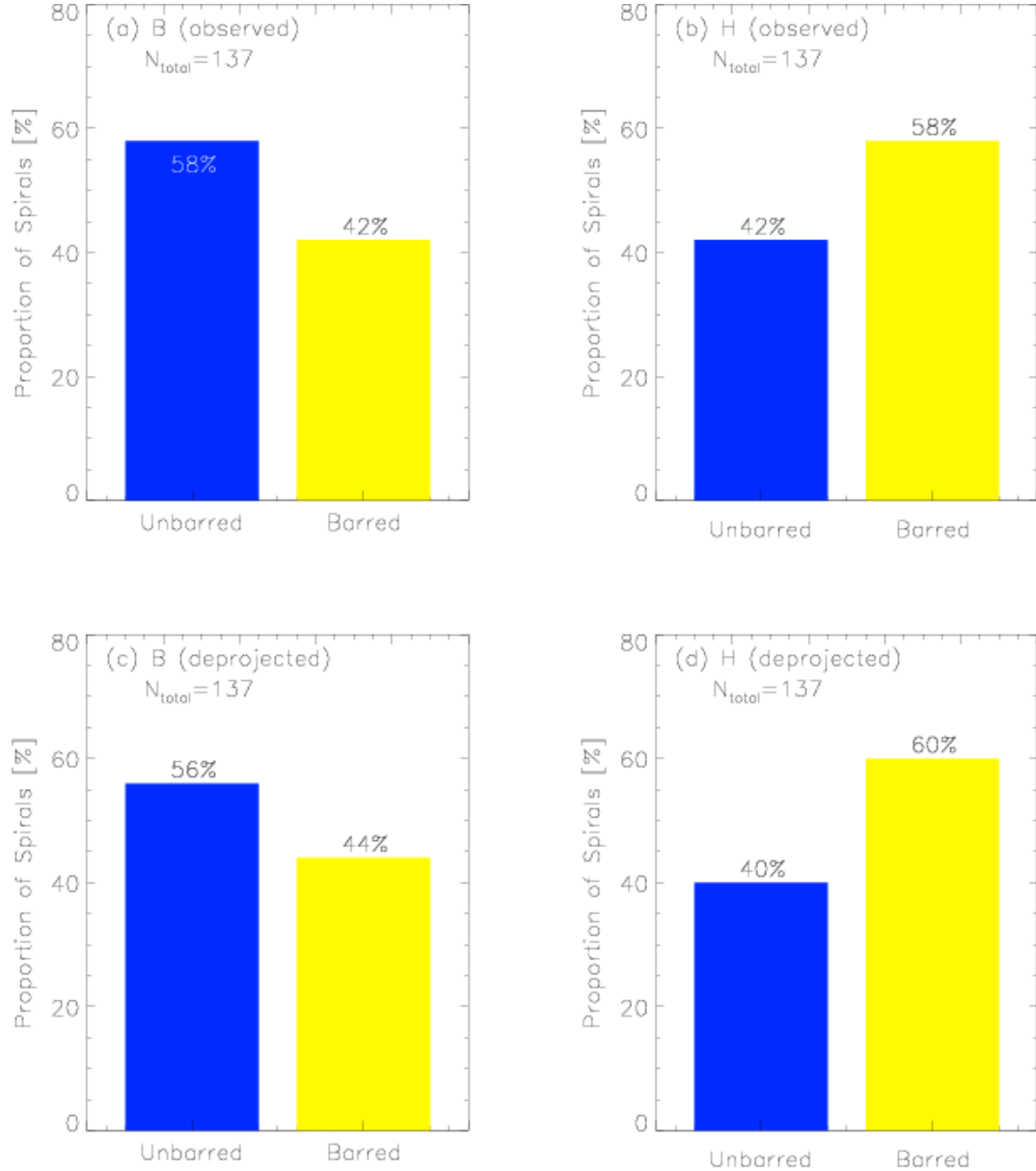


FIG. 8.— **The optical and NIR bar fraction at $z \sim 0$ from OSUBSGS:** We show the fraction of spirals that are barred in the B and H bands, based on ellipse fits of 137 moderately inclined galaxies (sample S4), followed by quantitative characterization of the resulting radial profiles of (e , SB, PA). Top row: The observed bar fraction before deprojection is 42% in the B band (left) and 58% in the H band (right). Bottom row: The deprojected bar fraction is 44% in the B band (left) and 60% in the H band (right).

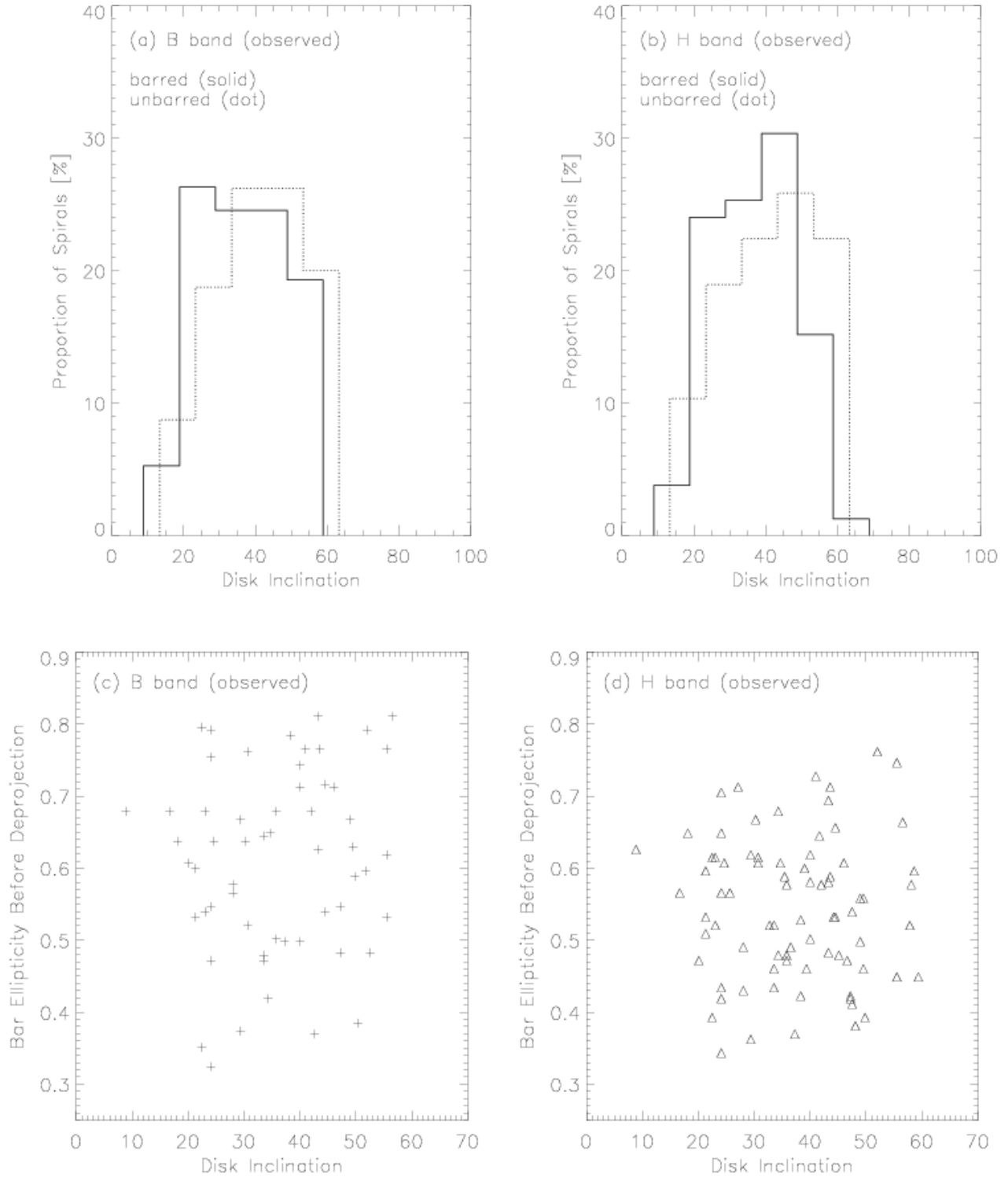


FIG. 9.— **Verifying that bar properties measured prior to deprojection are not biased by galaxy inclination:** Top tow: The histograms show the distributions of inclination i for galaxies that were classified as ‘barred’ or ‘unbarred’, prior to deprojection, in the B band (left) and H band (right). Note that there is no correlation with i . Bottom row: The measured bar ellipticity e_{bar} in the B band (left) and H band (right), prior to deprojection, are plotted against the galaxy inclination i . Note that there is no correlation between e_{bar} and i .

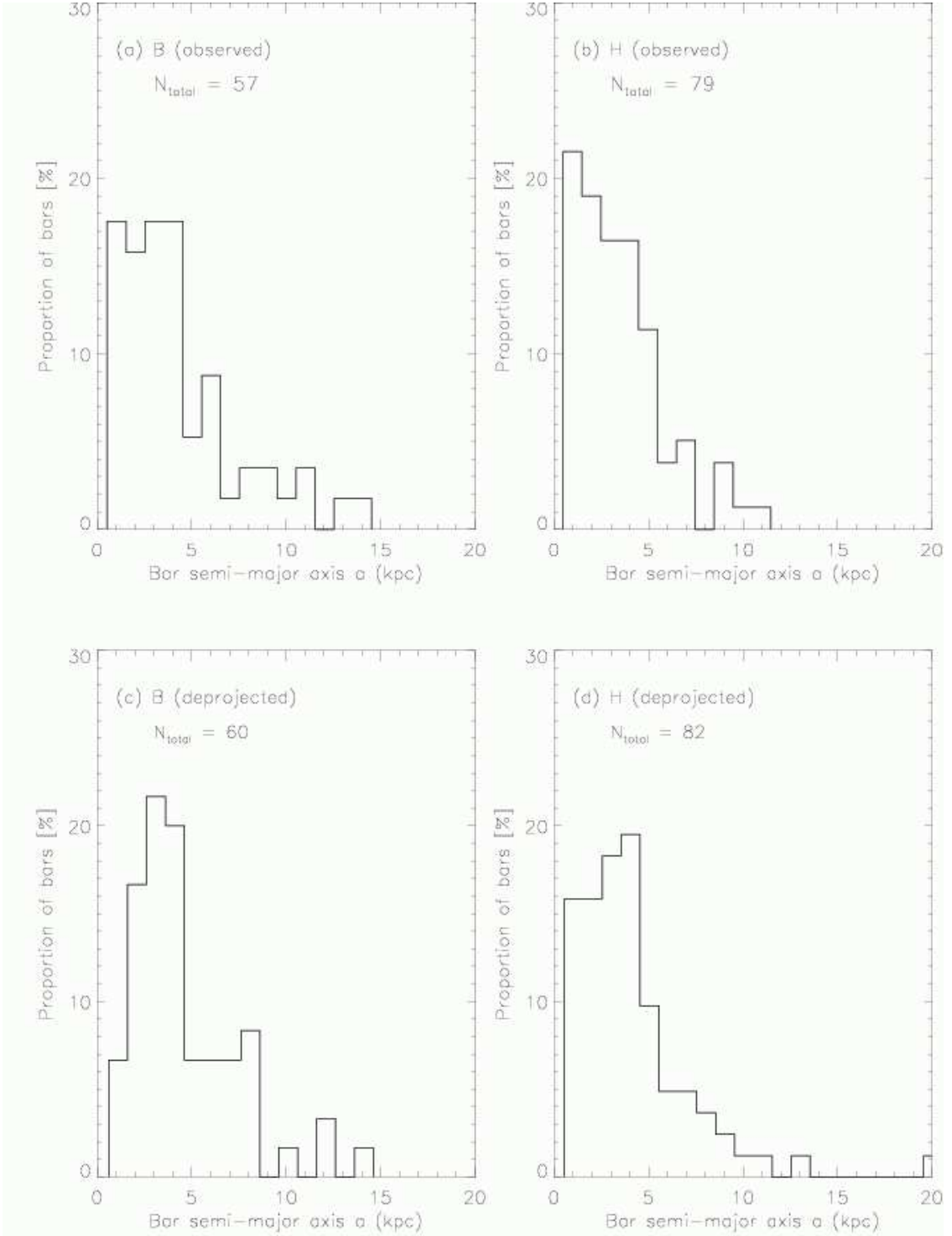


FIG. 10.— **Distribution of bar sizes at $z \sim 0$ from OSUBSGS:** The distributions of bar semi-major axes (a_{bar}) before (top row) and after (bottom row) deprojection are shown, for the B (left) and H (right) bands. Most (72% in B and 76% in H) bars have $a_{\text{bar}} \leq 5$ kpc, and $\sim 50\%$ of them cluster in the range 2 to 5 kpc. Deprojection makes several bars appear somewhat larger, but does not otherwise produce a large change in the overall shape of the distributions.

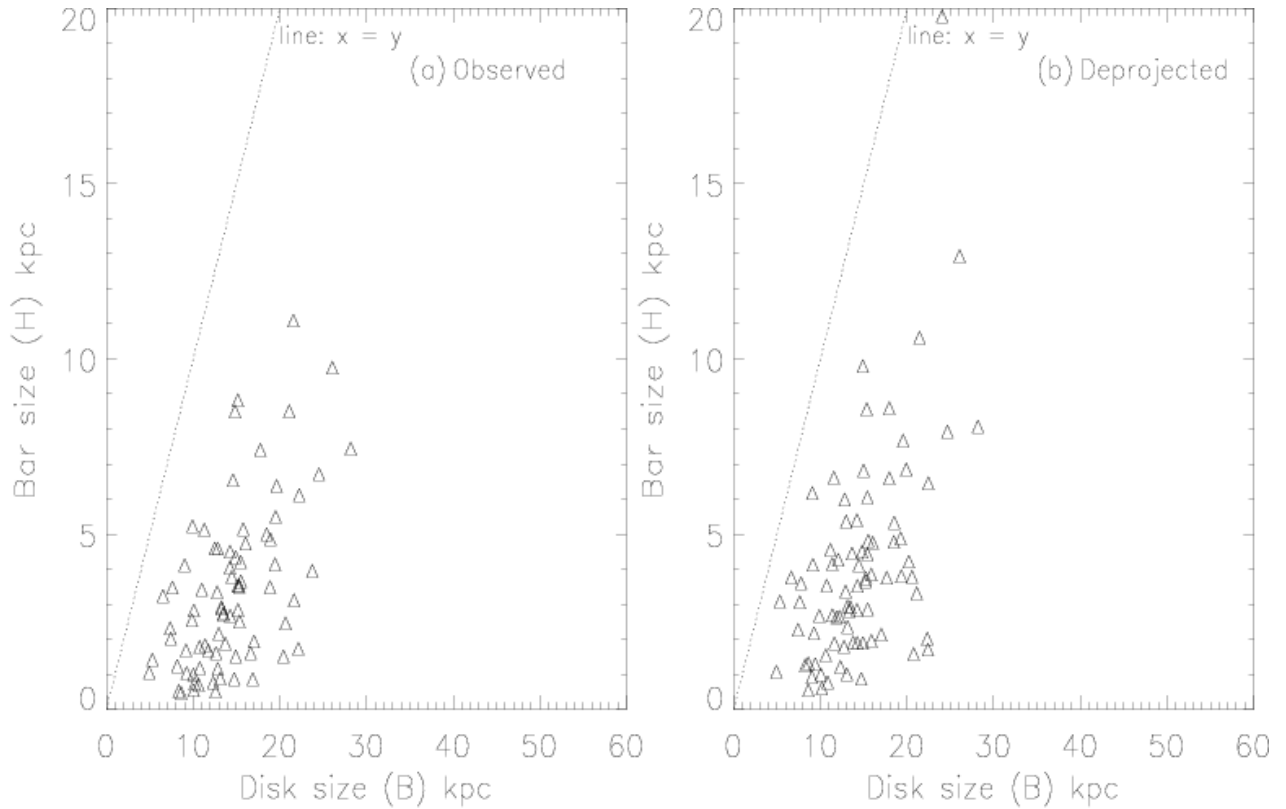


FIG. 11.— **Relationship between H band bar size and disk size at $z \sim 0$ from OSUBSGS:** The bar semi-major axis in the H band is plotted versus the disk size before (top row) and after (bottom row) deprojection. The disk size is measured in the B band image which is deeper than the H band and traces the disk further out. The deprojected bar and disk sizes are correlated with an average slope of ~ 0.9 . However, there is a large scatter of several kpc in bar size at a given disk size. For comparison, the dotted line has slope of 1.

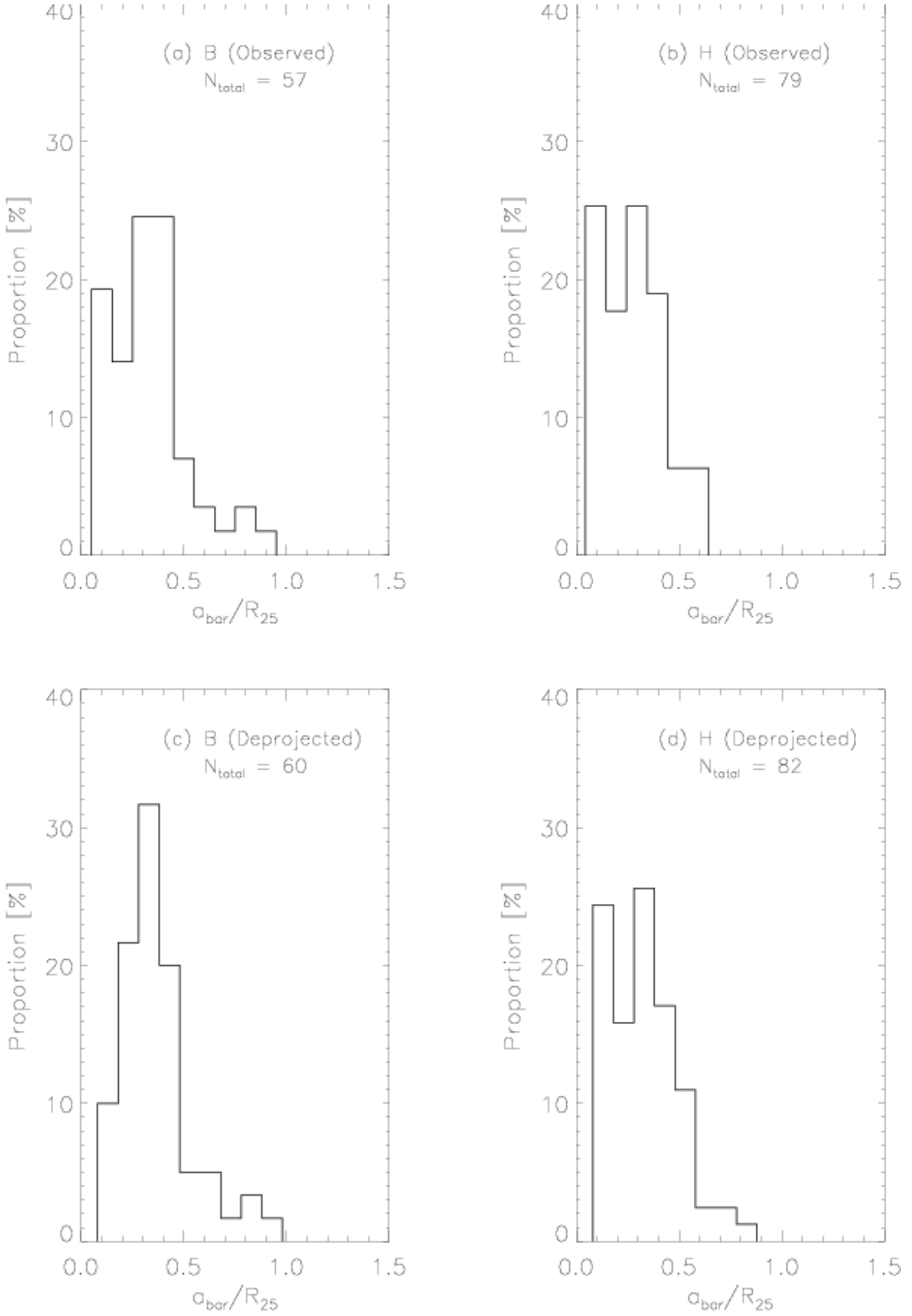


FIG. 12.— **Relationship between bar size and R_{25} at $z \sim 0$ from OSUBSGS:** The ratio of the bar semi-major axis (a_{bar}) to the isophotal radius (R_{25}) where the B -band surface brightness is $25 \text{ mag arcsec}^{-2}$ is shown before (top row) and after (bottom row) deprojection. In the left panels, the bar size (a_{bar}) is determined from the B band image and in the right panels from the H band image. We find that the ratio (a_{bar}/R_{25}) is always below 1.0, and lies primarily in the range 0.2 to 0.4 in both H and B bands.

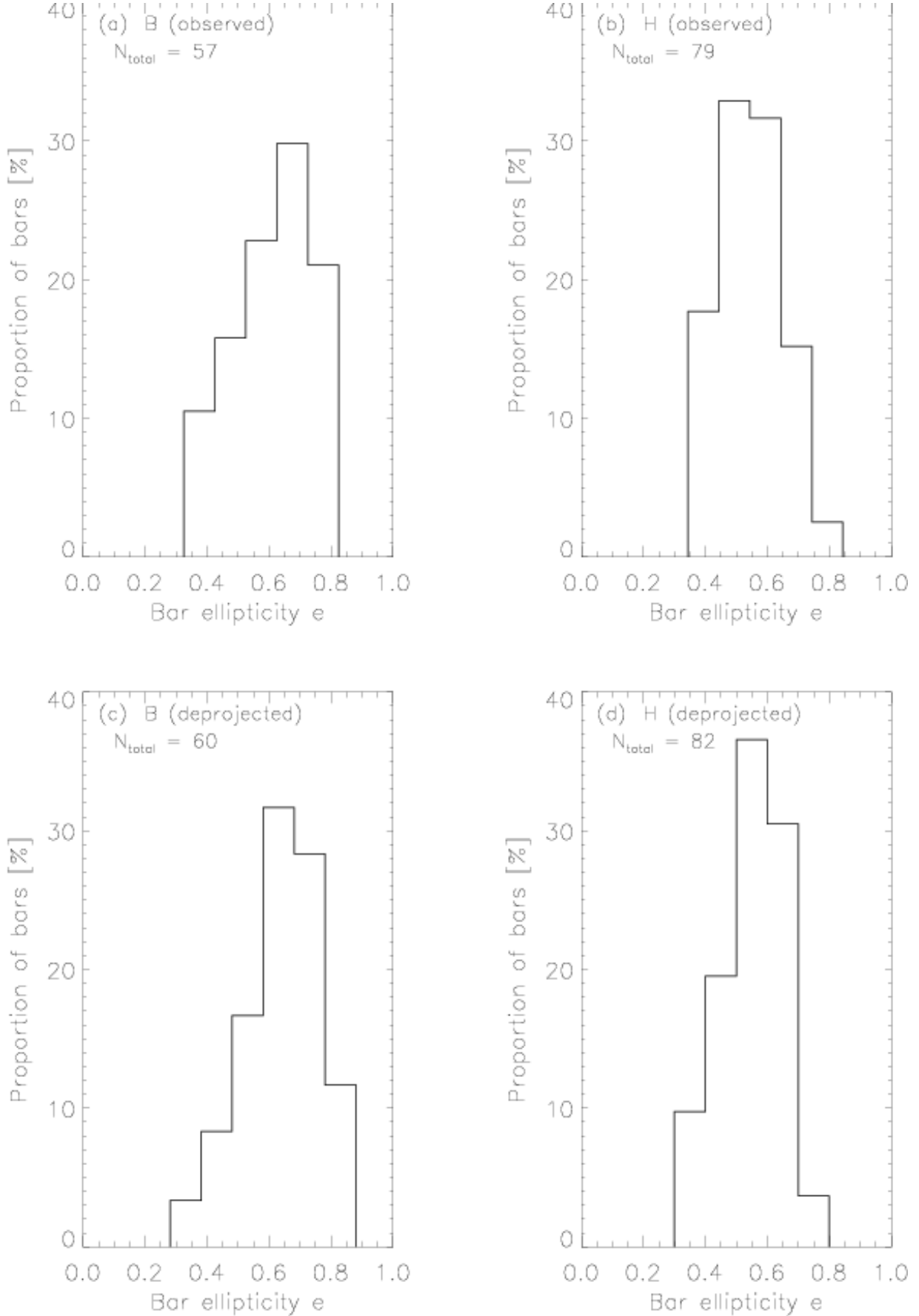


FIG. 13.— **Distributions of bar strengths at $z \sim 0$ from OSUBSGS:** The distributions of bar strengths (e_{bar}) before (top row) and after (bottom row) deprojection, in the B (left) and H (right) bands are shown. It is striking in that only a tiny fraction (7% in B ; 10% in H) of bars are very weak with e_{bar} between 0.25-to 0.40, while the majority of bars (70% in B ; 71% in H) seem to have moderate to high strengths, with e_{bar} between 0.50 to 0.75. Furthermore, we find no evidence for bimodality in the distribution of bar strength in the B or H bands.

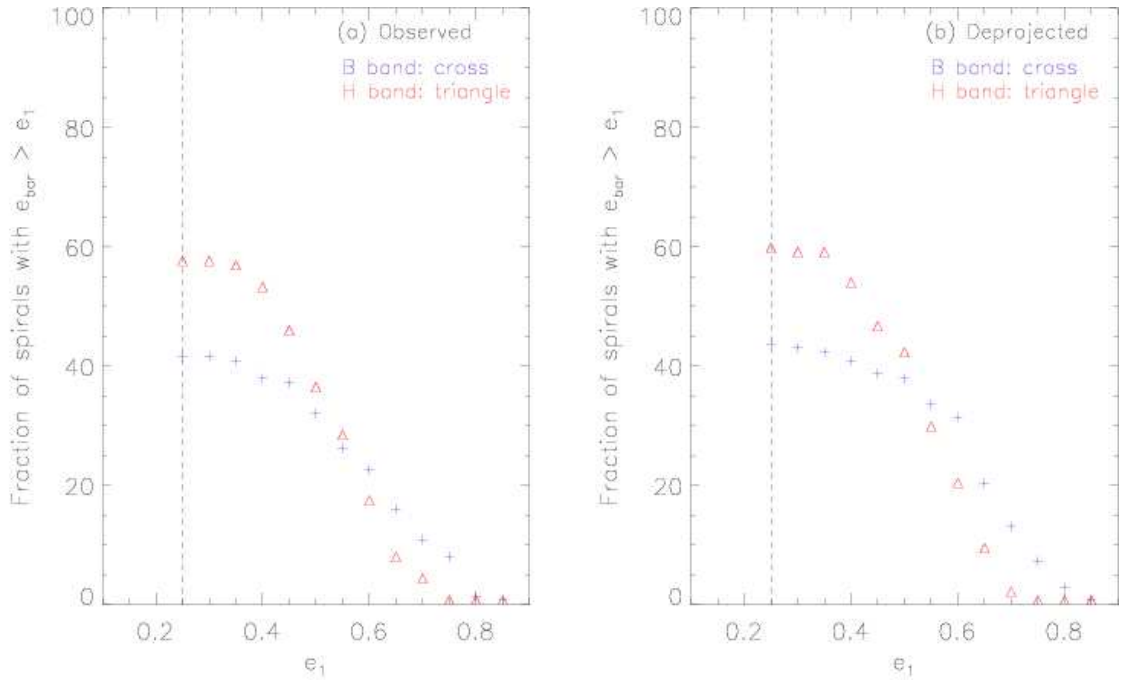


FIG. 14.— **Bar fraction as a function of bar strength:** A generalized plot of the fraction of disks with ‘strong’ and ‘weak’ bars is shown before (left panel) and after (right panel) deprojection. The y-axis shows the fraction of spiral galaxies that host bars whose strength e_{bar} exceeds a value e_1 in the B (cross) and H (triangle) bands. Along the x-axis, e_1 is varied. As e_1 rises from 0.35 to 0.45, 0.55, and 0.75, the deprojected bar fraction in the B -band falls from 42% to 39%, 34%, and 7%, respectively, while the bar fraction in the H -band falls from 59% to 47%, 30%, and 1%. The flattening of the curve around $e_1 \sim 0.45$ reflects the paucity of very weak bars with $0.25 \geq e_{\text{bar}} \leq 0.40$, while the steep fall in the curve for e_1 in the range 0.50–0.75 shows the preponderance of ‘strong’ bars.

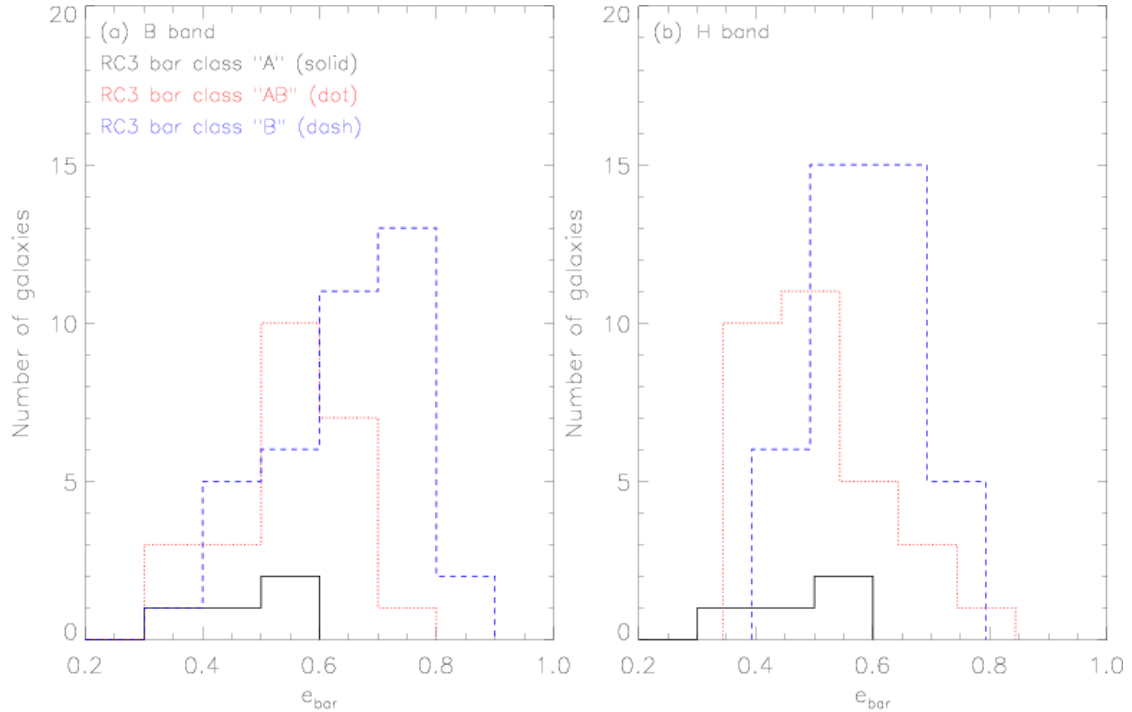


FIG. 15.— **A comparison of RC3 visual bar classes with e_{bar} from ellipse fits:** This figure shows the RC3 visual bar classes for all those galaxies in sample S4 that we classified as barred based on ellipse fits (§ 3.3 and § 3.4). The x-axis shows the bar strength or ellipticity e_{bar} , derived from ellipse fits in the B (left panel) and H (right panel) bands, prior to deprojection. The three RC3 visual bar classes are based on visual inspection of optical images (de Vaucouleurs et al. 1991) and classes ‘A’ (solid line), ‘AB’ (dotted line), and ‘B’ (dashed line) denote ‘unbarred’, ‘weakly barred’, and ‘strongly barred’ disks, respectively. In the B band, we find that 7%, 34%, and 79%, respectively, of the sample galaxies with RC3 visual classes of ‘A’, ‘AB’, and ‘B’, host bars. In the H band, the corresponding numbers are 18%, 64%, and 84%, respectively. Thus, many galaxies that are classified as unbarred in RC3 turn out to be barred and vice-versa. The mean bar strength e_{bar} is higher for RC3 visual class “B” than for class “AB”, but the two classes have significant overlap in the range $e_{\text{bar}} \sim 0.5\text{--}0.7$.

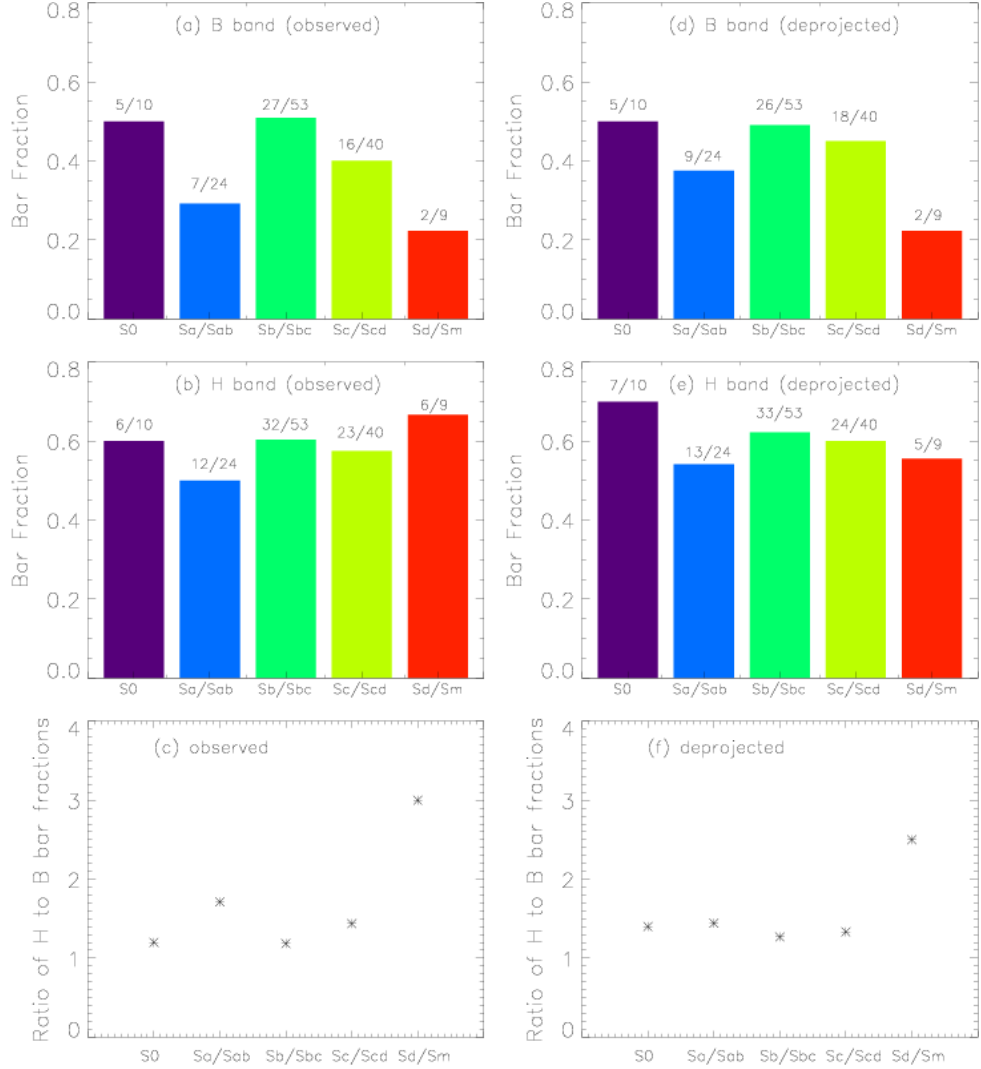


FIG. 16.— **Bar fraction as a function of Hubble type at $z \sim 0$ from OSUBSGS:** This figure shows what proportion of spirals with different Hubble types host bars. The bar fractions in the B band (top row) and H band (middle row) are shown as a function of RC3 Hubble types, before (left) and after (right) deprojection. The bar fraction above each bin is explicitly spelled out as the ratio (no of barred disks with a given Hubble type/total no of disks of a given Hubble type). The H band bar fraction remains high and $\sim 60\%$ across different Hubble types. The bottom row shows the ratio of the H band bar fraction to the B -band bar fraction before (left) and after (right) deprojection. In the B band, we find that the bar fraction is lower with respect to the H band by ~ 1.2 – 1.5 for S0s to Scs, and by ~ 2.5 for Sds/Sms. This is likely due to extinction, especially in the dusty, gas-rich late type (Scds–Sms) galaxies.

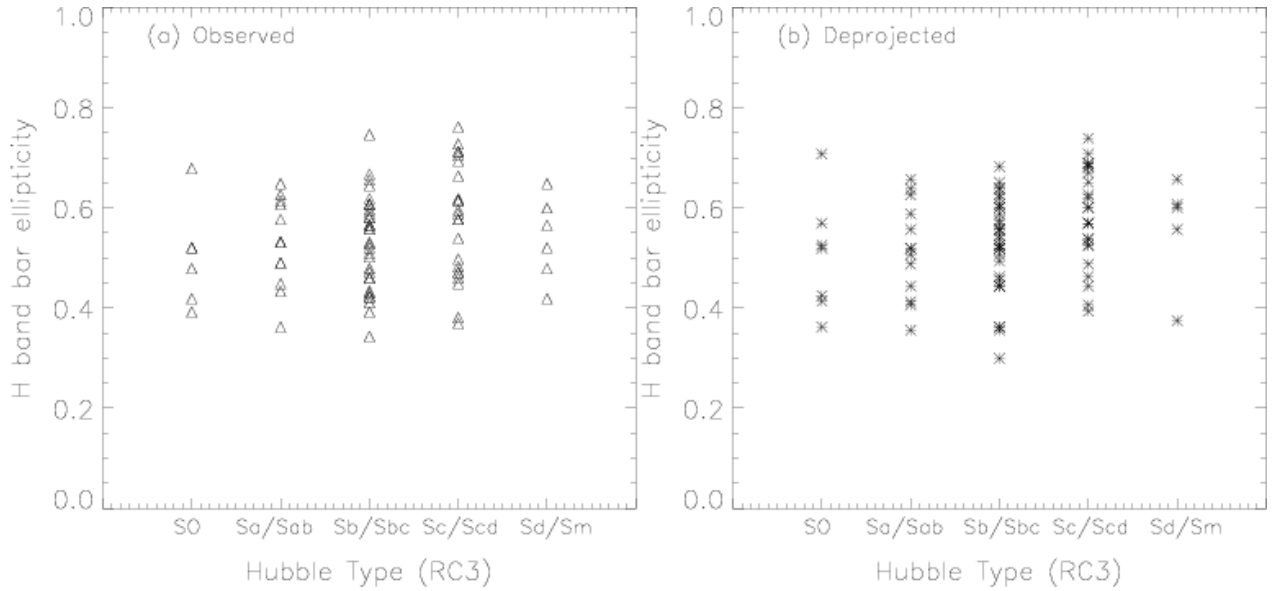


FIG. 17.— **Bar strength (e_{bar}) as a function of Hubble type at $z \sim 0$ from OSUBSGS:** The bar strength or ellipticity e_{bar} in the H band is plotted as a function of Hubble types before (left) and after (right) deprojection. The Hubble types are from RC3 and are binned as in Figure 16. Before deprojection, the number of galaxies in each Hubble type bin is: SO = 6, Sa/Sab = 12, Sb/Sbc = 32, Sc/Scd = 23, Sd/Sm = 6. After deprojection, the corresponding numbers are SO = 7, Sa/Sab = 13, Sb/Sbc = 33, Sc/Scd = 24, Sd/Sm = 5. The bar strength e_{bar} lies in the range 0.35–0.80, and shows no systematic variation across Hubble types either before or after deprojection.

TABLE 1
GLOBAL PROPERTIES OF SAMPLE S3 (169 GALAXIES) WITH ELLIPSE FITS IN B AND H

Galaxy Name (1)	Hubble Type (RC3) (2)	Bar Type (RC3) (3)	D (Mpc) (4)	D_{25} (') (5)	B_T (mag) (6)	M_V (mag) (7)	L_{IR} ($\log(L_\odot)$) (8)	L_B ($\log(L_\odot)$) (9)
Moderately inclined galaxies (N=137)								
IC 0239	SAB(rs)cd	AB	14.2	5.4	11.8	-19.66	-	9.81
IC 4444	SAB(rs)bc	AB	26.9	1.4	12	-20.79	10.53	10.33
IC 5325	SAB(rs)bc	AB	18.1	2.7	11.83	-20.02	-	9.83
NGC 0157	SAB(rs)bc	AB	20.9	3	11	-21.19	10.52	10.53
NGC 0210	SAB(s)b	AB	20.3	4.9	11.6	-20.65	-	10.22
NGC 0278	SAB(rs)b	AB	11.8	2.7	11.47	-19.53	10.03	10.04
NGC 0289	SAB(rs)bc	AB	19.4	8.3	11.72	-20.45	10.03	10.17
NGC 0428	SAB(s)m	AB	14.9	4.6	11.91	-19.4	-	9.85
NGC 0488	SA(r)b	A	29.3	5.4	11.15	-22.05	-	10.74
NGC 0685	SAB(r)c	AB	15.2	3.9	11.95	-19.42	-	9.8
NGC 0864	SAB(rs)c	AB	20	4.4	11.4	-20.66	-	10.27
NGC 1042	SAB(rs)cd	AB	16.7	4.4	11.56	-20.09	-	10.16
NGC 1058	SA(rs)c	A	9.1	3.6	11.82	-18.6	-	9.34
NGC 1073	SB(rs)c	B	15.2	5	11.47	-19.94	-	9.97
NGC 1084	SA(s)c	A	17.1	3.4	11.31	-20.43	10.54	10.3
NGC 1087	SAB(rs)c	AB	19	3.7	11.46	-20.45	10.26	10.28
NGC 1187	SB(r)c	B	16.3	5.4	11.34	-20.28	10.18	10.1
NGC 1241	SB(rs)b	B	26.6	3.6	11.99	-20.98	-	10.12
NGC 1300	SB(rs)bc	B	18.8	6.8	11.11	-20.94	-	10.36
NGC 1302	(R)SB(r)0	B	20	3.8	11.6	-20.8	-	10.24
NGC 1309	SA(s)bc	A	26	2.8	11.97	-20.54	10.24	10.26
NGC 1317	SAB(r)a	AB	16.9	3.1	11.91	-20.12	-	9.87
NGC 1350	(R')SB(r)ab	B	16.9	5	11.16	-20.85	-	10.18
NGC 1371	SAB(rs)a	AB	17.1	6.8	11.57	-20.49	-	10.08
NGC 1385	SB(s)cd	B	17.5	4.6	11.45	-20.28	10.18	10.1
NGC 1493	SB(r)cd	B	11.3	3.9	11.78	-19	-	9.58
NGC 1559	SB(s)cd	B	14.3	3.3	11	-20.13	10.21	10.24
NGC 1617	SB(s)a	B	13.4	4	11.38	-20.2	-	10.08
NGC 1637	SAB(rs)c	AB	8.9	5.1	11.47	-18.92	9.46	9.52
NGC 1703	SB(r)b	B	17.4	3.5	11.9	-19.86	-	-
NGC 1792	SA(rs)bc	A	13.6	6.1	10.87	-20.48	10.33	10.24
NGC 1832	SB(r)bc	B	23.5	2.6	11.96	-20.53	10.28	10.26
NGC 2139	SAB(rs)cd	AB	22.4	2.9	11.99	-20.12	10.16	10.16
NGC 2196	(R')SA(s)a	A	28.8	2.9	11.82	-21.29	-	10.46
NGC 2566	(R')SB(rs)ab pec	B	21.1	4.3	11.83	-20.6	10.6	-
NGC 2775	SA(r)ab	A	17	4.6	11.03	-21.02	-	10.24
NGC 2964	SAB(r)bc	AB	21.9	3	11.99	-20.39	10.36	10.15
NGC 3166	SAB(rs)0	AB	22	3.2	11.32	-21.32	9.94	10.28
NGC 3169	SA(s)a pec	A	19.7	5	11.08	-21.24	10.18	10.37
NGC 3223	SA(s)b	A	38.1	3.6	11.79	-21.93	-	10.88
NGC 3227	SAB(s)a pec	AB	20.6	5.9	11.1	-21.29	10.13	10.26
NGC 3261	SB(rs)b	B	33.4	3.9	12	-	-	10.64
NGC 3275	SB(r)ab	B	42.4	2.8	11.8	-	-	10.61
NGC 3423	SA(s)cd	A	10.9	4	11.59	-19.05	-	9.66
NGC 3504	(R)SAB(s)ab	AB	26.5	2.6	11.82	-20.99	10.72	10.34
NGC 3507	SB(s)b	B	19.8	3.2	11.73	-	-	10.23
NGC 3513	SB(rs)c	B	17	3.2	11.93	-19.65	-	9.98
NGC 3583	SB(s)b	B	34	2.6	11.9	-	10.54	10.61
NGC 3593	SA(s)0	A	5.5	4.8	11.86	-17.78	9.22	9
NGC 3596	SAB(rs)c	AB	23	4.1	11.95	-	-	10.32
NGC 3646	Ring	-	55.8	3.9	11.78	-22.6	-	-
NGC 3681	SAB(r)bc	AB	24.2	2.9	11.9	-20.73	-	10.06
NGC 3684	SA(rs)bc	A	23.4	2.9	12	-20.47	-	10.07
NGC 3686	SB(s)bc	B	23.5	2.9	11.89	-20.54	-	10.17
NGC 3726	SAB(r)c	AB	17	5.5	10.91	-20.73	9.78	10.33
NGC 3810	SA(rs)c	A	16.9	3.8	11.35	-20.37	10.12	10.24
NGC 3885	SA(s)0	A	27.8	2.9	11.89	-21.28	10.27	10.29
NGC 3887	SB(r)bc	B	19.3	3.4	11.41	-	9.8	10.16
NGC 3893	SAB(rs)c	AB	17	4.3	11.16	-	10.2	10.3
NGC 3938	SA(s)c	A	17	4.9	10.9	-20.77	9.93	10.3
NGC 3949	SA(s)bc	AB	17	2.8	11.54	-20.06	9.87	10.16
NGC 4027	SB(s)dm	B	25.6	3.3	11.66	-20.92	10.36	10.41
NGC 4030	SA(s)bc	A	25.9	4	11.42	-	10.64	10.3
NGC 4051	SAB(rs)bc	AB	17	5.4	10.83	-20.97	9.9	10.29
NGC 4123	SB(r)c	B	16.5	4.6	11.98	-19.71	9.76	10.29
NGC 4136	SAB(r)c	AB	9.7	4	11.69	-	-	9.48
NGC 4145	SAB(rs)d	AB	20.7	5.9	11.78	-20.31	-	10.28
NGC 4151	(R')SAB(rs)ab	AB	20.3	6.3	11.5	-20.77	10.2	10.38
NGC 4212	SAc	A	16.8	2.3	11.83	-19.97	9.82	10.02
NGC 4242	SAB(s)dm	AB	7.5	5.2	11.37	-18.55	-	9.36
NGC 4254	SA(s)c	A	16.8	5	10.44	-	10.54	10.53
NGC 4303	SAB(rs)bc	AB	15.2	5.9	10.18	-21.26	10.51	10.48
NGC 4314	SB(rs)a	B	9.7	4.2	11.43	-19.35	-	9.65
NGC 4394	(R)SB(r)b	B	16.8	3.4	11.73	-20.25	-	9.99
NGC 4414	SA(rs)c	A	9.7	4.5	10.96	-19.81	10.56	9.84

TABLE 1—Continued

Galaxy Name (1)	Hubble Type (RC3) (2)	Bar Type (RC3) (3)	D (Mpc) (4)	D_{25} ($''$) (5)	B_T (mag) (6)	M_V (mag) (7)	L_{IR} ($\log(L_\odot)$) (8)	L_B ($\log(L_\odot)$) (9)
NGC 4450	SA(s)ab	A	16.8	5	10.9	-21.05	-	10.34
NGC 4457	(R)SAB(s)0	AB	17.4	3.2	11.76	-20.29	-	10.01
NGC 4487	SAB(rs)cd	AB	19.9	3.9	11.63	-	-	10.27
NGC 4496	SB(rs)m	B	13.1	3.7	11.94	-19.17	-	9.8
NGC 4504	SA(s)bc	A	19.5	3.3	11.89	-	-	10.17
NGC 4548	SB(rs)b	B	16.8	5	10.96	-20.98	-	10.3
NGC 4571	SA(r)d	A	16.8	3.6	11.82	-19.82	-	9.94
NGC 4579	SAB(rs)b	AB	16.8	5.4	10.48	-21.47	9.87	10.46
NGC 4580	SAB(rs)a pec	AB	25.6	2.5	11.83	-	-	9.97
NGC 4593	(R)SB(rs)b	B	39.5	3.3	11.67	-	-	10.82
NGC 4618	SB(rs)m	B	7.3	3.1	11.22	-18.54	-	9.44
NGC 4643	SB(rs)0	B	25.7	2.9	11.72	-21.29	-	10.39
NGC 4647	SAB(rs)c	AB	16.8	2.8	11.94	-19.84	9.81	9.93
NGC 4651	SA(rs)c	A	16.8	3.6	11.39	-20.31	9.72	10.22
NGC 4665	SB(s)0	B	17.9	4.2	10.5	-	-	9.94
NGC 4689	SA(rs)bc	A	16.8	3.7	11.6	-20.18	-	10.04
NGC 4691	(R)SB(s)0 pec	B	22.5	3.5	11.66	-20.68	10.32	10.24
NGC 4698	SA(s)ab	A	16.8	3.3	11.46	-20.58	-	10.22
NGC 4699	SAB(rs)b	AB	25.7	3.1	10.41	-22.53	10.12	10.89
NGC 4775	SA(s)d	A	26.6	2.3	11.67	-	-	10.32
NGC 4900	SB(rs)c	B	17.3	2.5	11.9	-19.82	9.73	9.83
NGC 4902	SB(r)b	B	39.2	2.6	11.61	-22.05	-	10.65
NGC 4930	SB(rs)b	B	35	5.4	12	-21.62	-	-
NGC 4939	SA(s)bc	A	44.3	5.6	11.9	-21.97	-	11.16
NGC 4941	(R)SAB(r)ab	AB	6.4	4.2	11.9	-17.97	-	9.12
NGC 4995	SAB(rs)b	AB	28	2.3	12	-21.11	-	10.4
NGC 5005	SAB(rs)bc	AB	21.3	5.6	10.61	-21.83	10.46	10.7
NGC 5054	SA(s)bc	A	27.3	4.6	11.67	-21.27	10.46	10.66
NGC 5078	SA(s)a sp	A	27.1	4	12	-21.2	10.5	-
NGC 5085	SA(s)c	A	28.9	3.9	11.96	-	-	10.48
NGC 5101	(R)SB(rs)0	B	27.4	5.4	11.63	-21.54	-	10.57
NGC 5121	(R')SA(s)a	A	22.1	2.2	11.51	-21.16	-	10.08
NGC 5247	SA(s)bc	A	22.2	4.6	10.5	-21.77	10.32	10.57
NGC 5334	SB(rs)c	B	24.7	4.2	11.99	-	-	10.06
NGC 5371	SAB(rs)bc	AB	37.8	4.2	11.32	-22.27	10.67	10.82
NGC 5427	SA(s)c pec	A	38.1	2.3	11.93	-21.54	10.8	10.57
NGC 5483	SA(s)c	A	24.7	4.6	11.93	-	10.05	10.3
NGC 5676	SA(rs)bc	A	34.5	4	11.87	-21.5	10.63	10.77
NGC 5701	(R)SB(rs)0	B	26.1	4.2	11.76	-21.2	-	10.33
NGC 5713	SAB(rs)bc pec	AB	30.4	3.1	11.84	-21.21	10.72	10.43
NGC 5850	SB(r)b	B	28.5	4.6	11.54	-21.52	-	10.47
NGC 5921	SB(r)bc	B	25.2	4.9	11.49	-21.18	-	10.46
NGC 5962	SA(r)c	A	31.8	2.8	11.98	-21.17	10.55	10.46
NGC 6215	SA(s)c	A	20.5	1.9	12	-20.1	10.54	10.53
NGC 6300	SB(rs)b	B	14.3	5.2	10.98	-20.58	10.09	10.32
NGC 6384	SAB(r)b	AB	26.6	6.3	11.14	-21.7	-	10.72
NGC 6753	(R)SA(r)b	A	40.9	2.5	11.97	-21.92	10.89	-
NGC 6782	(R)SAB(r)a	AB	50.8	2.2	11.84	-	-	-
NGC 6902	SA(r)b	A	35.7	6.8	11.64	-21.83	-	10.33
NGC 6907	SB(s)bc	B	43	3.3	11.9	-21.96	11.03	-
NGC 7083	SA(s)bc	A	38.7	3.2	11.87	-21.72	10.45	10.73
NGC 7205	SA(s)bc	A	20.5	3.2	11.55	-20.61	10.07	10.3
NGC 7213	SA(s)a	A	22	2.1	11.01	-21.59	-	10.34
NGC 7217	(R)SA(r)ab	A	16	3.6	11.02	-20.9	9.9	10.34
NGC 7412	SB(s)b	B	21.1	4.3	11.88	-20.27	-	10.12
NGC 7418	SAB(rs)cd	AB	17.8	3.6	11.65	-	10.01	9.96
NGC 7479	SB(s)c	B	32.4	3.9	11.6	-21.7	10.79	10.64
NGC 7552	(R')SB(s)ab	B	19.5	3.5	11.25	-20.88	11.03	10.25
NGC 7713	SB(r)d	B	8.2	4.6	11.51	-18.38	-	9.58
NGC 7723	SB(r)b	B	23.7	3.9	11.94	-20.66	-	10.31
NGC 7727	SAB(s)a pec	AB	23.3	3.3	11.5	-21.25	-	10.34
NGC 7741	SB(s)cd	B	12.3	4.1	11.84	-19.14	-	9.7

Highly inclined galaxies with $i > 60^\circ$ (N=32)

IC 4402	SA(s)b sp	A	22.9	5	12	-20.24	10.05	-
IC 5052	SBd sp	B	6.7	5	11.16	-18.6	9.28	
NGC 0625	SB(s)m sp	B	3.9	5	11.91	-16.61	8.57	8.73
NGC 0779	SAB(r)b	AB	17.3	4.4	11.95	-20.03	-	10.2
NGC 0908	SA(s)c	A	17.8	6.1	10.83	-21.07	10.27	10.51
NGC 1003	SA(s)cd	A	10.7	6.3	12	-18.7	-	9.64
NGC 1421	SAB(rs)bc	AB	25.5	3.5	11.95	-20.61	10.25	10.64
NGC 1808	(R)SAB(s)a	AB	10.8	7.6	10.74	-20.24	10.71	10
NGC 1964	SAB(s)b	AB	20	6.1	11.58	-20.7	10.09	10.37
NGC 2090	SA(rs)c	A	10.2	6.8	11.99	-18.84	-	9.61
NGC 2280	SA(s)cd	A	23.2	6.8	10.9	-21.53	10.13	10.6
NGC 3511	SA(s)c	A	15.5	6.8	11.53	-19.99	9.82	10.25
NGC 3675	SA(s)b	A	12.8	5.8	11	-	9.92	10.13

TABLE 1—*Continued*

Galaxy Name (1)	Hubble Type (RC3) (2)	Bar Type (RC3) (3)	D (Mpc) (4)	D_{25} ($''$) (5)	B_T (mag) (6)	M_V (mag) (7)	L_{IR} ($\log(L_\odot)$) (8)	L_B ($\log(L_\odot)$) (9)
NGC 3705	SAB(r)ab	AB	17	4.6	11.86	-20.08	-	10.25
NGC 3877	SA(s)c	A	17	5.1	11.79	-20.16	9.89	10.29
NGC 4062	SA(s)c	A	9.7	4.5	11.9	-18.79	-	9.5
NGC 4100	(P)SA(rs)bc	A	17	5.1	11.89	-19.99	10.04	10.25
NGC 4293	(R)SB(s)0	B	17	6.3	11.26	-20.79	-	10.21
NGC 4388	SA(s)b	A	16.8	5.6	11.76	-20.11	10	10.16
NGC 4448	SB(r)ab	B	9.7	3.8	12	-18.86	-	9.56
NGC 4527	SAB(s)bc	AB	13.5	6.3	11.38	-20.13	10.42	10.08
NGC 4654	SAB(rs)cd	AB	16.8	4.8	11.1	-20.63	10.1	10.32
NGC 4666	SABc	AB	14.1	4.2	11.49	-20.01	10.36	10.1
NGC 4772	SA(s)a	A	16.3	2.8	11.96	-20.02	-	9.7
NGC 4818	SAB(rs)ab pec	AB	21.5	3.4	12	-20.55	9.75	10.46
NGC 4856	SB(s)0	B	21.1	3.8	11.49	-21.12	-	10.3
NGC 5161	SA(s)c	A	33.5	6.1	12	-21.42	-	10.64
NGC 5448	(R)SAB(r)a	AB	32.6	4	11.93	-	-	10.47
NGC 7184	SB(r)c	B	34.1	6.1	11.65	-21.81	-	10.73
NGC 7582	(R')SB(s)ab	B	17.6	4.5	11.37	-20.61	10.87	10.26
NGC 7606	SA(s)b	A	28.9	5.2	11.51	-21.55	-	10.7
NGC 7814	SA(s)ab: sp	AB	16	5.5	11.56	-20.45	-	10.18

Note. — Columns are : (1) Galaxy name; (2) Hubble type from RC3 (de Vaucouleurs et al. 1991); (3) RC3 bar type, which is based on visual inspection of optical images and runs as ‘B’=‘strongly barred’, ‘AB’=‘weakly barred’, and ‘A’=‘unbarred’; (4) Distance in Mpc. Most values are from the NBG (Tully 1988), which assumes a Hubble constant of $75 \text{ km s}^{-1} \text{ Mpc}^{-1}$. Exceptions are NGC 6753, NGC 6782, NGC 5078, NGC 6907, NGC 7814, and ESO 142-19, for which distances from RC3 are used; (5) D_{25} in arcminutes, the diameter of the isophote where the B band surface brightness is 25 magnitude arcsecond $^{-2}$. Values are from the NBG, except for NGC 6753, NGC 6782, NGC 5078, NGC 6907, NGC 7814, and ESO 142-19 where RC3 data are used; (6) B_T , the total blue magnitude from RC3; (7) M_V , the absolute V magnitude from RC3; (8) L_{IR} , the global IR luminosity ($8 - 1000 \mu\text{m}$) in units of $\log(L_\odot)$, from the IRAS Revised Bright Galaxy Sample (Sanders et al. 2003); (9) L_B , the global blue luminosity in units of $\log(L_\odot)$, from the RC3.

TABLE 2
BAR STATISTICS FROM SAMPLE S4 (137 GALAXIES)

Band	Unbarred	Barred
<i>B</i> (observed)	80 = 58%	57 = 42%
<i>H</i> (observed)	58 = 42%	79 = 58%
<i>B</i> (deprojected)	77 = 56%	60 = 44%
<i>H</i> (deprojected)	55 = 40%	82 = 60%

Note. — Columns are : (1) Band (observed or deprojected); (2) Number and fraction of galaxies classified as unbarred; (3) Number and fraction of galaxies classified as barred.

TABLE 3
STRUCTURAL PROPERTIES OF SAMPLE S4 (137 GALAXIES) IN B AND H

Galaxy Name	i ($^{\circ}$)	PA_{disk}	class (B)	e_{bar} (B)	a_{bar} (B) (kpc)	class (H)	e_{bar} (H)	a_{bar} (H) (kpc)
(1)	(2)	(3)	(4)	(5)	(6)	(7)	(8)	(9)
IC 0239	37.25	171.62	u	-	-	-	-	-
IC 4444	36.53	77.39	u	-	-	u	-	-
IC 5325	38.31	34.23	u	-	-	b	0.52	1.54
NGC 0157	41.67	43.03	u	-	-	u	-	-
NGC 0210	49.53	160.18	b	0.62	12.34	b	0.49	9.79
NGC 0278	25.65	161.94	u	-	-	u	-	-
NGC 0289	35.43	162.82	u	-	-	b	0.6	2.13
NGC 0428	47.22	109.97	u	-	-	u	-	-
NGC 0488	38.73	6.05	u	-	-	u	-	-
NGC 0685	35.8	95.88	b	0.68	2.08	b	0.6	1.28
NGC 0864	43.27	31.57	b	0.71	4.21	b	0.6	3.53
NGC 1042	40.35	173.4	b	0.68	4.62	b	0.69	4.45
NGC 1058	13.32	79.15	u	-	-	u	-	-
NGC 1073	24.1	174.28	b	0.77	4.24	b	0.71	4.55
NGC 1084	39.35	58.88	u	-	-	b	0.41	6.17
NGC 1087	52.59	4.27	u	-	-	u	-	-
NGC 1187	30.68	130.22	b	0.72	3.55	b	0.57	2.92
NGC 1241	55.52	151.37	b	0.66	3.82	b	0.63	4.14
NGC 1300	55.52	102.03	b	0.62	8.47	b	0.57	8.56
NGC 1302	22.47	13.09	b	0.31	2.9	b	0.36	2.93
NGC 1309	21.31	64.18	u	-	-	u	-	-
NGC 1317	29.39	171.62	b	0.44	0.6	b	0.44	0.6
NGC 1350	58.1	2.51	u	-	-	b	0.59	6.81
NGC 1371	24.1	81.79	u	-	-	b	0.41	1.91
NGC 1385	47.51	24.54	b	0.82	2.03	b	0.65	1.78
NGC 1493	21.31	90.6	u	-	-	b	0.57	1.26
NGC 1559	56.56	61.54	b	0.8	1.74	b	0.53	0.92
NGC 1617	58.1	109.97	u	-	-	u	-	-
NGC 1637	35.8	31.57	b	0.54	1.22	b	0.49	1.07
NGC 1703	30.68	134.64	u	-	-	b	0.36	1.31
NGC 1792	50.38	139.03	u	-	-	b	0.52	4.27
NGC 1832	48.96	11.33	b	0.6	2.54	b	0.44	2.27
NGC 2139	36.53	154.89	u	-	-	u	-	-
NGC 2196	45.13	57.12	u	-	-	u	-	-
NGC 2566	24.63	59.76	b	0.62	4.97	b	0.56	4.78
NGC 2775	24.63	24.54	u	-	-	u	-	-
NGC 2964	49.82	95.88	b	0.68	2.62	b	0.58	2.64
NGC 3166	56.04	77.39	u	-	-	b	0.52	3.8
NGC 3169	55.52	58.88	u	-	-	u	-	-
NGC 3223	47.22	117.03	u	-	-	u	-	-
NGC 3227	55.52	151.37	u	-	-	u	-	-
NGC 3261	28.04	59.76	b	0.58	5.48	b	0.44	3.75
NGC 3275	21.31	150.49	b	0.6	7.67	b	0.52	6.6
NGC 3423	39.35	35.99	u	-	-	u	-	-
NGC 3504	8.84	79.15	b	0.69	3.84	b	0.63	4.13
NGC 3507	21.31	67.69	b	0.54	2.98	b	0.51	2.67
NGC 3513	43.27	63.3	b	0.8	2.77	b	0.74	2.17
NGC 3583	39.35	134.64	u	-	-	b	0.53	4.43
NGC 3593	57.85	86.18	u	-	-	u	-	-
NGC 3596	32.34	81.79	u	-	-	u	-	-
NGC 3646	56.04	56.24	u	-	-	u	-	-
NGC 3681	24.1	132.88	b	0.28	1.13	b	0.3	0.99
NGC 3684	47.22	127.58	u	-	-	u	-	-
NGC 3686	33.53	18.36	b	0.7	2.75	b	0.54	2.62
NGC 3726	52.04	13.96	b	0.71	4	b	0.68	3.84
NGC 3810	45.73	17.48	u	-	-	u	-	-
NGC 3885	58.86	114.37	u	-	-	u	-	-
NGC 3887	44.52	13.09	b	0.62	3.71	b	0.53	3.36
NGC 3893	48.1	10.45	u	-	-	b	0.54	6.05
NGC 3938	30.25	13.96	u	-	-	u	-	-
NGC 3949	16.67	143.43	u	-	-	u	-	-
NGC 4027	38.73	176.03	u	-	-	b	0.66	1.21
NGC 4030	43.59	21.9	u	-	-	u	-	-
NGC 4051	30.25	116.13	b	0.61	4.25	b	0.64	4.81
NGC 4123	43.59	121.42	b	0.69	10.57	b	0.63	4.21
NGC 4136	20.09	51.84	b	0.61	1.72	b	0.46	0.77
NGC 4145	57.85	98.52	b	0.64	1.45	b	0.56	1.7
NGC 4151	36.53	2.51	u	-	-	b	0.52	7.93
NGC 4212	43.59	72.97	u	-	-	b	0.44	2.86
NGC 4242	45.13	22.78	u	-	-	b	0.37	3.08
NGC 4254	24.63	59.76	u	-	-	u	-	-
NGC 4303	30.68	144.31	b	0.7	3.35	b	0.59	4.5
NGC 4314	18.12	38.63	b	0.66	3.26	b	0.66	3.76
NGC 4394	24.1	109.97	b	0.53	4.04	b	0.56	3.6
NGC 4414	44.21	166.34	u	-	-	u	-	-
NGC 4450	44.21	174.28	b	0.41	3.86	b	0.41	3.65
NGC 4457	25.65	86.18	u	-	-	u	-	-
NGC 4487	48.96	72.97	u	-	-	b	0.39	1

TABLE 3—Continued

Galaxy Name (1)	i ($^{\circ}$) (2)	PA_{disk} (3)	class (B) (4)	e_{bar} (B) (5)	a_{bar} (B) (kpc) (6)	class (H) (7)	e_{bar} (H) (8)	a_{bar} (H) (kpc) (9)
NGC 4496	24.1	65.94	b	0.77	2.17	b	0.61	0.87
NGC 4504	55.52	147.85	u	-	-	u	-	-
NGC 4548	40.02	154.89	b	0.6	6.29	b	0.61	5.99
NGC 4571	33.53	36.87	u	-	-	u	-	-
NGC 4579	35.8	95.88	b	0.49	3.96	b	0.46	3.75
NGC 4580	43.27	161.94	b	0.61	4.3	b	0.36	1.96
NGC 4593	43.27	105.57	b	0.67	13.64	b	0.62	12.94
NGC 4618	25.65	178.99	u	-	-	b	0.6	0.54
NGC 4643	34.3	56.24	b	0.52	7.18	b	0.57	5.4
NGC 4647	50.38	121.42	b	0.6	2.54	u	-	-
NGC 4651	49.53	71.21	u	-	-	u	-	-
NGC 4665	33.53	17.48	b	0.39	3.88	b	0.43	4.11
NGC 4689	44.21	173.4	u	-	-	u	-	-
NGC 4691	34.3	27.18	u	-	-	b	0.71	2.01
NGC 4698	59.36	174.28	u	-	-	b	0.51	2.68
NGC 4699	33.53	34.23	b	0.38	1.74	b	0.36	1.58
NGC 4775	18.12	47.45	u	-	-	u	-	-
NGC 4900	22.47	113.49	b	0.81	5.42	b	0.62	1.88
NGC 4902	16.67	102.92	b	0.69	6.83	b	0.54	4.75
NGC 4930	40.02	52.72	b	0.53	8.16	b	0.44	8.07
NGC 4939	53.93	6.93	u	-	-	u	-	-
NGC 4941	58.86	13.96	u	-	-	u	-	-
NGC 4995	47.51	93.24	b	0.63	6.36	b	0.56	3.78
NGC 5005	59.36	59.76	u	-	-	u	-	-
NGC 5054	52.59	159.3	u	-	-	u	-	-
NGC 5078	48.96	148.73	u	-	-	u	-	-
NGC 5085	32.34	56.24	u	-	-	u	-	-
NGC 5101	23.03	65.94	b	0.56	7.39	b	0.53	6.84
NGC 5121	48.96	57.12	u	-	-	u	-	-
NGC 5247	36.53	36.87	u	-	-	u	-	-
NGC 5334	41.99	11.33	b	0.67	3.06	b	0.57	1.89
NGC 5371	40.35	31.57	b	0.53	6.5	b	0.46	19.78
NGC 5427	38.31	11.33	u	-	-	b	0.53	4.88
NGC 5483	34.68	50.09	u	-	-	u	-	-
NGC 5676	59.86	50.09	u	-	-	u	-	-
NGC 5701	24.1	43.03	b	0.43	5.81	b	0.41	5.33
NGC 5713	32.74	1.63	u	-	-	b	0.6	3.52
NGC 5850	29.39	178.99	b	0.71	12.1	b	0.64	10.6
NGC 5921	46.03	130.22	b	0.78	8.52	b	0.68	7.67
NGC 5962	42.63	109.97	u	-	-	u	-	-
NGC 6215	44.21	43.03	u	-	-	b	0.54	1.89
NGC 6300	38.31	109.09	b	0.77	3	b	0.52	2.84
NGC 6384	55.26	27.18	u	-	-	u	-	-
NGC 6753	30.68	25.42	u	-	-	u	-	-
NGC 6782	28.04	36.87	b	0.56	6.74	b	0.49	6.45
NGC 6902	22.47	162.82	u	-	-	b	0.36	3.31
NGC 6907	51.76	65.94	u	-	-	u	-	-
NGC 7083	54.73	8.69	u	-	-	u	-	-
NGC 7205	58.61	65.94	u	-	-	u	-	-
NGC 7213	18.12	179.87	u	-	-	u	-	-
NGC 7217	30.68	136.4	u	-	-	u	-	-
NGC 7412	52.59	74.73	b	0.61	1.88	b	0.65	6.61
NGC 7418	27.11	91.48	b	0.78	2.68	b	0.68	2.81
NGC 7479	41.02	33.35	b	0.71	8	b	0.67	8.6
NGC 7552	23.03	33.35	b	0.71	2.07	b	0.64	5.36
NGC 7713	59.86	166.34	u	-	-	u	-	-
NGC 7723	34.68	38.63	b	0.6	3.21	b	0.56	2.35
NGC 7727	16.67	64.18	u	-	-	u	-	-
NGC 7741	40.02	167.22	b	0.79	3.24	b	0.69	3.06

Note. — Columns are : (1) Galaxy name; (2) Outer disk inclination i , calculated from B band ellipse fits before deprojection; (3) Outer disk PA, calculated from B band ellipse fits before deprojection; (4) B band classification as unbarred (u) or barred (b) from ellipse fits after deprojection; (5) Bar strength e_{bar} of large-scale bar in B band after deprojection; (6) Bar semi-major axis a_{bar} in kpc of large-scale bar in B band after deprojection; (7) H band classification as unbarred (u) or barred (b) from ellipse fits after deprojection; (8) Bar strength e_{bar} of large-scale bar in H band after deprojection; (9) Bar semi-major axis a_{bar} in kpc of large-scale bar in H band after deprojection.